



Full length article

A creep-resistant additively manufactured Al-Ce-Ni-Mn alloy[☆]

Richard A. Michi^{a,*}, Kevin Sisco^b, Sumit Bahl^a, Ying Yang^a, Jonathan D. Poplawsky^c, Lawrence F. Allard^a, Ryan R. Dehoff^d, Alex Plotkowski^a, Amit Shyam^a

^a Materials Science and Technology Division, Oak Ridge National Laboratory, Oak Ridge, TN, USA

^b Department of Mechanical, Aerospace, and Biomedical Engineering, University of Tennessee, Knoxville, TN, USA

^c Center for Nanophase Materials Sciences, Oak Ridge National Laboratory, Oak Ridge, TN, USA

^d Manufacturing Science Division, Oak Ridge National Laboratory, Oak Ridge, TN, USA

ARTICLE INFO

Article history:

Received 31 August 2021

Revised 25 January 2022

Accepted 29 January 2022

Available online 3 February 2022

Keywords:

Additive manufacturing

Aluminum alloys

High-temperature materials

Creep

Al-Ce-Ni-Mn alloy

ABSTRACT

Existing additively manufactured aluminum alloys exhibit poor creep resistance due to coarsening of their strengthening phases and refined grain structures. In this paper, we report on a novel additively manufactured Al-10.5Ce-3.1Ni-1.2Mn wt.% alloy which displays excellent creep resistance relative to cast high-temperature aluminum alloys at 300–400 °C. The creep resistance of this alloy is attributed to a high volume fraction (~35%) of submicron intermetallic strengthening phases which are coarsening-resistant for hundreds of hours at 350 °C. The results herein demonstrate that additive manufacturing provides opportunities for development of creep-resistant aluminum alloys that may be used in bulk form in the 250–400 °C temperature range. Pathways for further development of such alloys are identified.

© 2022 Acta Materialia Inc. Published by Elsevier Ltd. All rights reserved.

1. Introduction

Consideration of creep deformation in aluminum (Al) alloys is critical for long-lifetime component design, especially in the growing number of applications which take advantage of the relatively high thermal and electrical conductivities of Al. As the application space for additive manufacturing (AM) of Al increases, it is therefore important to understand how AM processing affects creep behavior, especially in the 200–450 °C temperature range where AM Al alloys are targeted as replacements for denser and/or more expensive steels and Ti alloys [1]. The creep resistances of a few studied AM Al alloys are not promising. In a study of AM Al-2.9Mg-2.1Zr (wt.%) crept at 260 °C (0.57 T_m, where T_m is the absolute melting temperature of Al), the creep threshold stress decreased by ~65%, from ~40 to ~14 MPa, after either a peak aging treatment at 400 °C or *in-situ* aging during creep at 260 °C [2]. The

authors attributed the drop in threshold stress to grain boundary sliding enabled by the coarsening and subsequent reduced pinning effectiveness of grain boundary particles. The Al-2.9Mg-2.1Zr alloy contained regions of equiaxed grains with submicron diameters (~0.8 μm), and the resulting high density of grain boundaries also likely contributed to grain boundary sliding. In a study of AM Al-10Mg-0.3Si (wt.%) at 225 °C (0.53 T_m), creep deformation under applied compressive loads of 100–130 MPa resulted in strain rates of 1×10^{-7} – 7×10^{-6} s⁻¹ [3]. Under tension, strain rates of these magnitudes resulted in sample rupture within 65 h [4]. During deformation, the refined Si network formed upon AM fabrication coarsened and spheroidized, likely contributing to alloy weakening [5]. These existing studies highlight two concerns for creep of AM Al: (i) refined grain sizes that may be present in AM alloys from grain nucleation effects [6–12] which are likely to lead to grain boundary sliding, and (ii) the need for coarsening-resistant strengthening phases [1], which are not present in the most widely studied AM Al alloys i.e., those based on the Al-Si-(Mg) systems. Fortunately, new classes of Al alloys for AM offer opportunities for the design of materials with improved creep resistance.

A class of Al alloys designed for AM has emerged based on the principle that makes Al-Si-(Mg) resistant to hot tearing and thus popular for AM, i.e., the narrow solidification temperature range and large volume fraction of terminal eutectic which fills the interdendritic regions that are initiation sites for hot tearing [13]. These alloys are based primarily on the Al-Ce eutectic system [14–18], but also include those based on Al-Ni [19–21], Al-Fe [22–24],

* Notice: This manuscript has been authored by UT-Battelle, LLC under Contract No. DE-AC05-00OR22725 with the U.S. Department of Energy. The United States Government retains and the publisher, by accepting the article for publication, acknowledges that the United States Government retains a non-exclusive, paid-up, irrevocable, world-wide license to publish or reproduce the published form of this manuscript, or allow others to do so, for United States Government purposes. The Department of Energy will provide public access to these results of federally sponsored research in accordance with the DOE Public Access Plan (<https://www.energy.gov/downloads/doe-public-access-plan>)

* Corresponding author.

E-mail address: michira@ornl.gov (R.A. Michi).

and Al-Cu [25,26] eutectic systems. Apart from an inherent resistance to hot tearing, rapid solidification associated with AM processing refines the eutectic structures in these alloys, resulting in room-temperature mechanical properties comparable to that of AM Al-Si-(Mg). For example, the room-temperature yield strengths of as-fabricated binary AM Al-5.7Ni (wt.%) and Al-10Ce (wt.%) alloys were 278 ± 5 and 222 ± 2 MPa, respectively [18,21], whereas the yield strengths of as-fabricated AM Al-Si-(Mg) alloys are 200–300 MPa [27].

In addition to printability, the new eutectic-based alloys have another advantage. Unlike in the AM Al-Si-(Mg) alloys, the strengthening phases in several of the alloys are resistant to high-temperature coarsening, suggesting that they will possess excellent high-temperature mechanical properties. Since the eutectic AM alloys do not contain expensive elements such as Sc, they are a lower cost alternative to Al-Sc-based high-temperature alloys containing coarsening-resistant L₁₂-Al₃Sc nanoprecipitates [12,28]. The complex component shapes possible in AM also make the AM eutectic alloys a possible alternative to high-temperature rapidly solidified alloys such as the 8009 (Al-Fe-V-Si) alloys, which are dimensionally limited for component design since they are processed by consolidation of ribbons [29]. Several existing studies have demonstrated the potential of eutectic-based alloys for high-temperature use. Qi et al. reported an AM Al-2.5Fe alloy which retained 86% of its as-fabricated yield stress after exposure at 300 °C for 1000 h, attributed to thermal stability of nanometric metastable Al₆Fe strengthening precipitates [30,31]. Deng et al. reported a 300 °C yield strength of 137 ± 2 MPa for an AM Al-5.7Ni alloy, which is 66 MPa higher than AM Al-10Si-0.3Mg at the same temperature [4,21]. Although complex microstructural changes occur, the microhardness of a ternary eutectic AM Al-10Ce-8Mn alloy reported by Plotkowski et al. is stable for up to 200 h at 350–450 °C after an initial drop from the as-fabricated condition [16].

The AM Al-Ce-Ni-Mn alloy in the present study is based on the Al-Ce-Ni eutectic system. In the casting literature, ternary eutectic alloys based on this system have a high volume fraction (> 20%) of submicron Al₁₁Ce₃ and Al₃Ni precipitates which are coarsening-resistant up to ~400 °C [32,33], contributing to a retention of the as-cast hardness after aging up to ~400 °C. As this ternary eutectic system shows promise for high-temperature applications, it was chosen for AM studies, where the strength of eutectic-based alloys may be enhanced by microstructural refinement from high solidification velocities [34], as described by the Jackson-Hunt model [35]. The combination of coarsening resistance and a refined AM-processed microstructure is key for the high-temperature performance of the AM Al-Ce-Ni-Mn alloy as it is non heat-treatable, i.e., precipitation hardening is not expected, and the strength will only decrease as particle coarsening occurs during exposure to elevated temperatures [34].

Through microstructural analysis across multiple length scales combined with evaluations of ambient- and high-temperature mechanical properties, we show that the AM Al-Ce-Ni-Mn alloy is indeed a promising lightweight alloy for applications in the 250–400 °C temperature range. We find that the creep resistance is particularly outstanding at 300–400 °C when compared to traditional cast high-temperature alloys, an unexpected result considering the small grain sizes on the order of 10–100 μm. Considering the poor creep resistance noted in the few existing creep studies of AM Al alloys, the surprising results herein provide several important considerations for design of future creep-resistant AM aluminum alloys. Note that in this paper, we report mechanical properties only for loading parallel to the build direction. Although evaluations of potential anisotropy in material behavior are important for AM materials, we focus on a single build direction to study the fundamental strengthening and deformation mechanisms of the AM Al-Ce-Ni-Mn alloy.

Table 1

Summary of processing parameters used for LPBF fabrication of the Al-Ce-Ni-Mn alloy.

Laser Power (W)	Laser Speed (mm s ⁻¹)	Laser Spot Size (μm)	Hatch Spacing (mm)	Layer Thickness (μm)
370	1300	80	0.19	30

Table 2

Composition of AM Al-Ce-Ni-Mn alloy, as verified by inductively coupled plasma optical emission spectrometry (ICP-OES). Compositions are in wt.%.

Al	Ce	Ni	Mn	Si	Fe	Mg
84.92	10.50	3.09	1.18	0.12	0.18	0.01

2. Experimental procedures

2.1. Material processing

Eck industries (Manitowoc, WI) supplied cast Al-Ce-Ni-Mn ingots which were subsequently atomized using nitrogen gas by Connecticut Engineering Associates Corporation (Sandy Hook, CT). Volunteer Aerospace Inc. (Knoxville, TN) manufactured the Al-Ce-Ni-Mn alloy using an EOS M 290 laser powder bed fusion system, with processing parameters given in Table 1 and a 10 mm stripe scan strategy. These parameters resulted in built material without excessive porosity and were chosen from 49 different sets initially investigated. Cylindrical bars with length of 115 mm and diameter of 15 mm were built in an argon atmosphere with the long axes perpendicular to the build plate, which was heated to 200 °C to reduce residual thermal stresses. To further reduce residual stresses, the as-fabricated cylinders were subjected to a stress-relief anneal at 450 °C for 2 h prior to removal from the build plate. The composition of the resulting AM alloy is given in Table 2, as measured by inductively coupled plasma optical emission spectrometry (ICP-OES). We refer to the alloy herein as AM Al-Ce-Ni-Mn. Silicon, Fe, and Mg are impurities. All sample aging was performed in air, followed by an air cool.

2.2. Microstructural characterization

Scanning electron microscopy (SEM) imaging of the microstructure was performed using Hitachi S-4800 and Zeiss Gemini 450 SEMs. Electron backscatter diffraction (EBSD) imaging of the grain structure was performed in a TESCAN MIRA3 SEM equipped with an EDAX detector. A step size of 0.5 μm was used during EBSD mapping. SEM images were analyzed using Image J software for quantification of microstructural features. The reported average precipitate radius values were determined using a circular area equivalence. The total area of precipitates was first measured, then divided by the total number of precipitates to find the average precipitate area. The average circular area-equivalent radius was then calculated. Fracture surfaces were imaged using a Hitachi TM3030Plus SEM. Scanning transmission electron microscopy (STEM) imaging of the microstructure was performed at 200 kV using a JEOL 2200FS equipped with a CEOS GmbH (Heidelberg, Ger.) aberration corrector. Electron-transparent STEM foils of 3 mm diameter were prepared by dual-jet electropolishing (Struers A/S TenuPol) with an electrolyte of composition 25% HNO₃ – 75% methanol chilled to -13 °C. Nanotips for atom-probe tomography (APT) analysis were prepared in a dual-beam FEI Nova 200 focused ion beam (FIB)-SEM using a standard lift-out technique [36]. Wedges were extracted from polished samples using a Ga⁺ beam, attached to a Si micropost on a coupon, then sharpened using a 30 kV Ga⁺ beam to a ~100 nm minimum radius and cleaned and sharpened using a 2 kV Ga⁺ beam. APT experiments were

performed in voltage mode using a LEAP4000X HR tomograph (Cameca Instruments) at a specimen temperature of 70 K, 30% pulse fraction, 0.3% detection rate, and 200 kHz pulse rate. The APT data were reconstructed and analyzed using IVAS version 3.8 software (Cameca Instruments). Background-corrected matrix and precipitate compositions were extracted from the plateau regions of proximity histograms [37].

2.3. Mechanical testing

Tensile specimens with 6.35 mm gauge diameter and 31.75 mm gauge length were machined such that the loading axis was parallel to the build direction. Tensile tests were conducted per the ASTM E8 and E21 standards for ambient- and elevated-temperature tests, respectively. The initial strain-rate was 10^{-4} s $^{-1}$ and subsequently increased to 10^{-3} s $^{-1}$ at 1.5% strain for elevated-temperature tests per the ASTM E21 standard. Two replicates were tested at each temperature. Strain was measured by an axial extensometer with 25.4 mm gauge length placed in the gauge section of the tensile specimens. Creep samples were the same dimensions as the tensile specimens above, with the loading axis also parallel to the build direction. Tensile creep tests were performed in air at 300–400 °C, with tensile stresses applied using hanging dead loads. Sample elongation was taken as the average of two readings from a dual-gauge extensometer on the gauge section of the samples. Both single stress and stress step tests were performed. During single stress tests, a single load was applied to the sample until fracture. During stress step tests, once a steady-state strain rate was achieved for a given stress as measured from the slope of the strain vs. time curve, the load was increased to obtain an additional steady-state strain rate. This procedure was repeated until sample fracture or 10% total strain, whichever came first, so that a single specimen provided several minimum strain rate vs. stress data points. Some fractured tensile creep specimens were sectioned along the loading axis using wire electrical discharge machining (EDM) for examination of the microstructure after creep. Additional samples were sectioned from the gauge region of crept specimens for examination of dislocation structures after creep using STEM. Vickers microhardness measurements were performed on a plane parallel to the build direction using a 300 g load and 10 s dwell time. At least 30 measurements were taken across multiple grains on each sample to provide a statistically significant microhardness value.

2.4. Thermodynamic modeling

Computer coupling of phase diagrams and thermo-chemistry, i.e., the CALPHAD approach [38] was used to aid understanding of the as-fabricated microstructure. In this approach, the Gibbs energy of individual phases in the Al-Ce-Ni-Mn system was modeled based on the constituent unary, binary, and ternary systems. The Gibbs energy functions of the four unary systems Al, Ce, Ni and Mn were adopted from the SGTE (Scientific Group Thermodata Europe) database compiled by Dinsdale [39]. The Gibbs energy functions of binary phases were taken from Wang et al. [40] and Yang et al. [41]. The Gibbs energy functions of the Al-Ce-Ni system have been modeled by Wang et al. [40]. The Gibbs energy functions of the Al-Ce-Mn system were developed in our previous work [41]. Because of the small concentration of Mn and Ni in the current AM alloy, the Gibbs energy functions of ternary phases in Al-Mn-Ni and Ce-Mn-Ni were obtained through extrapolation of constituent binary phases. The currently developed Gibbs energy models for phases in Al-rich region of Al-Ce-Ni-Mn have been validated by experimental work. The detailed modeling process and the comparison between calculated and experimental data will be presented elsewhere [42].

This work will primarily present results focusing on the calculated solidification path to interpret the phases observed in the AM alloy, i.e., Al-10.5Ce-3.1Ni-1.2Mn (wt. %). The phase formation during solidification is a kinetic process. In this article, a simple solidification model, the Scheil model [43] is employed. The major assumptions in this model are: the solidified phases are “frozen,” i.e., no back diffusion is considered in the solid phases; diffusion in liquid phase is so fast that the liquid phase always has a uniform composition; and the phase equilibrium between the liquid and solid phases at the local interface is reached. The isobaric condition is also assumed throughout this article.

3. Results

3.1. As-stress-relieved (SR) microstructure

As discussed in the experimental procedures, the as-fabricated material underwent a stress-relief heat treatment for 2 h at 450 °C, denoted SR, prior to mechanical testing or further heat treatment. SEM-backscattered electron (BSE) images in Fig. 1a–b shows the microstructural changes that occur upon the SR treatment. A dendritic precipitate distribution in the as-fabricated condition evolves into a more homogeneous dispersion of precipitates within the dark-contrast matrix. Although significant spheroidization of the bright-contrast precipitates in the as-printed microstructure occurs, an average submicron precipitate diameter of 236 ± 58 nm is obtained in the as-SR state, and the volume fraction of precipitates is $\sim 35\%$. In the as-SR microstructure, melt pool boundaries (MPBs) from AM processing are evident, visible as arc-like features containing a lower number density of coarser precipitate phases (Fig. 1c–d). The MPBs form during AM processing as material is built up layer by layer. Formation of coarser phases at the MPBs may be due to several factors including slower solidification velocities at the MPBs or *in-situ* annealing from subsequent building of layers.

High-resolution STEM microscopy was utilized to analyze the as-SR microstructure, with samples taken from the grip section of a tensile specimen tested at room temperature. Since samples were taken from the grip section where the applied stress is reduced compared to the gauge section, the microstructure is considered representative of the as-SR state. The observed microstructure is shown in Fig. 2, along with complimentary EDS maps for majority species Ce, Ni, and Mn. The precipitate phases have a globular morphology and are arranged in a network that appears to have been broken up, likely by the SR heat treatment. The average precipitate size is on the scale of ~ 200 nm in diameter.

At least three types of precipitates observed: Ce-rich and Ni-rich precipitates form the broken-up precipitate network, while Mn-rich precipitates are embedded in the latter two. At higher magnifications under STEM, specific orientation relationships between the matrix and precipitate phases were not observed, suggesting that the precipitates are incoherent with the matrix. A representative STEM image showing the interface between the matrix and a Ce-rich precipitate is shown in Fig. 2e.

The as-SR microstructure was further investigated using atom-probe tomography (APT). Fig. 3 shows an example of a reconstructed APT volume in which an interface between a Mn-rich precipitate and a Ce-rich precipitate was analyzed. An enrichment of Si, reaching a maximum concentration of ~ 1 at.%, is noted near the interface. Thermodynamic calculations detailed in the supplementary information predict the presence of five precipitate phases: $\text{Al}_{11}\text{Ce}_3$, $\text{Al}_{10}\text{Mn}_2\text{Ce}$, $\text{Al}_{20}\text{Mn}_2\text{Ce}$, $\text{Al}_{23}\text{Ni}_6\text{Ce}_4$ and Al_3Ni . The first four phases match well with the phase compositions measured by APT as summarized in Table S1 of the supplementary information. Manganese is the only solute species measured at consistent and

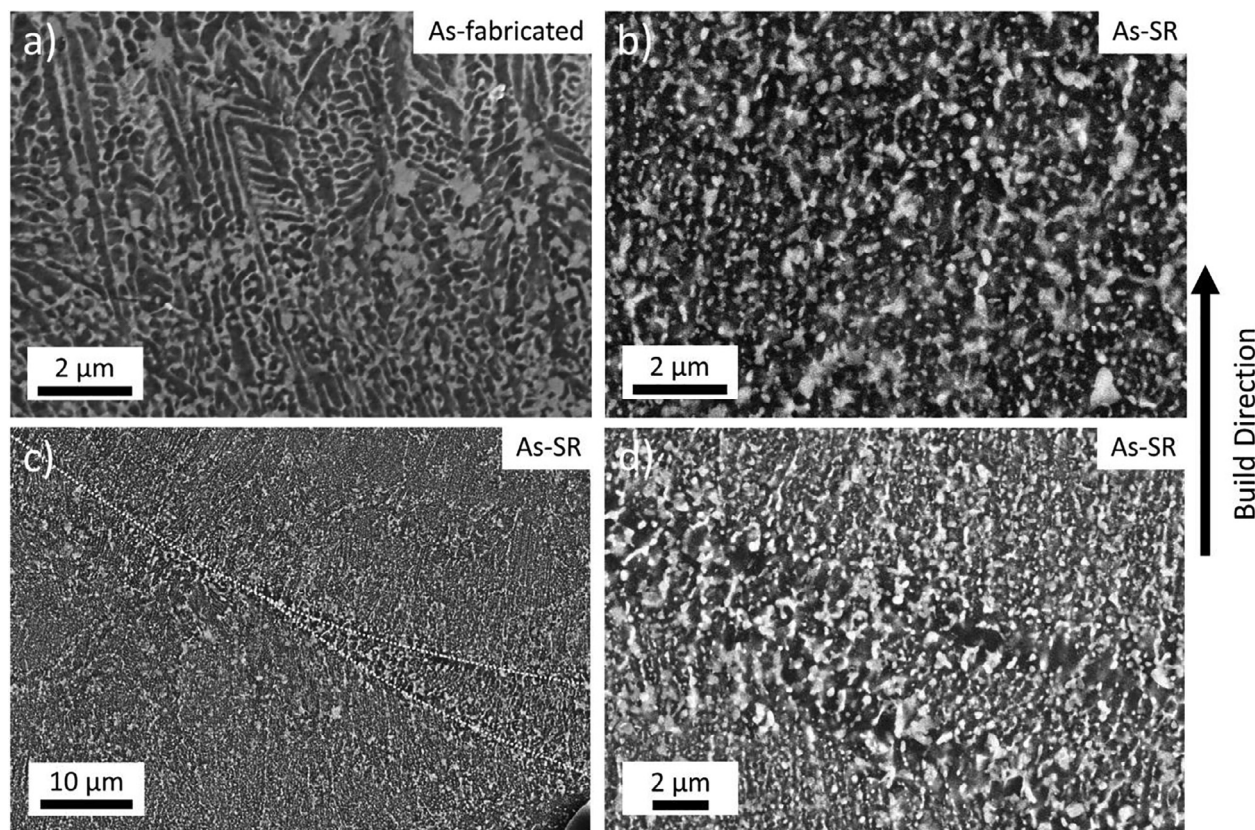


Fig. 1. SEM-BSE micrographs showing (a) dendritic microstructure of the as-fabricated material and (b-d) microstructural spheroidization after a stress-relief heat treatment at 450 °C for 2 h (as-SR). (c-d) Melt pool boundaries (MPBs), visible as regions of coarser precipitate phases, are present in the as-SR microstructure. MPBs are outlined by white dotted lines in (c) and shown in detail in (d).

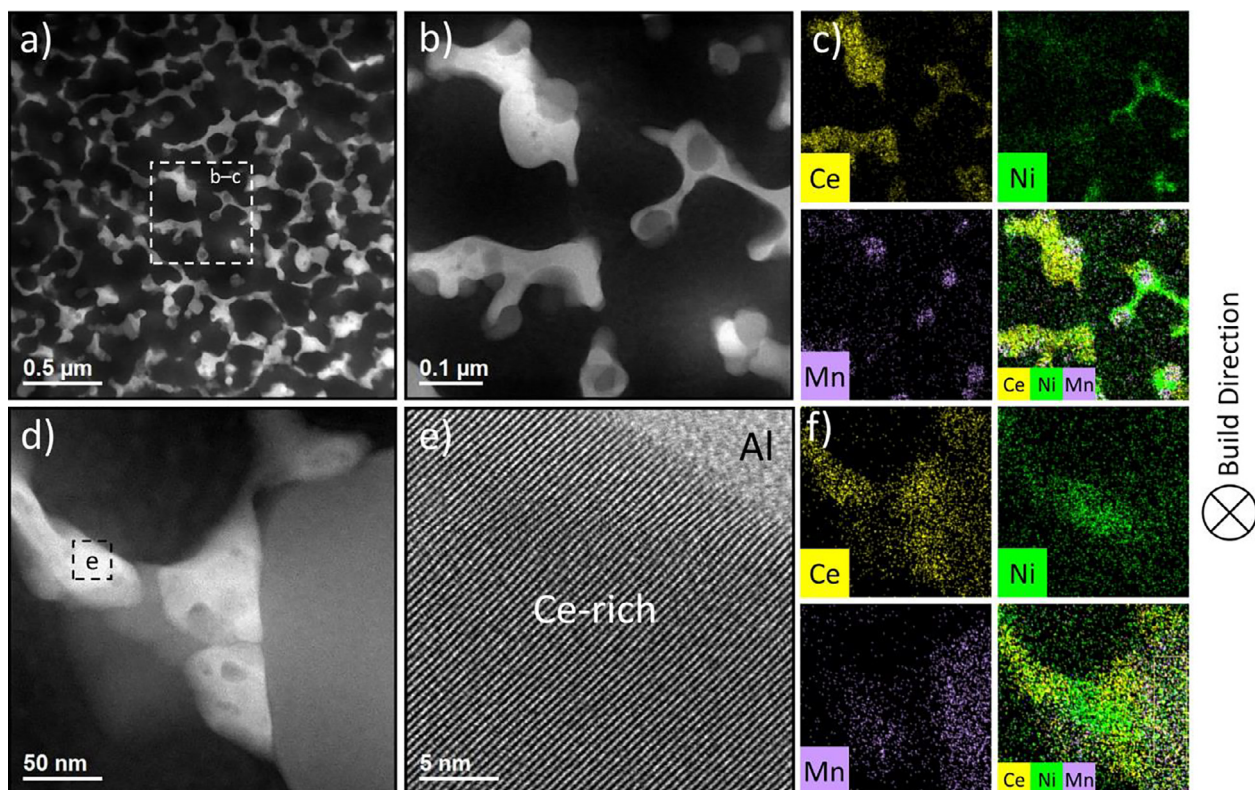


Fig. 2. (a-c) Dark-field STEM micrographs of the as-SR microstructure with associated EDS maps. The microstructure consists of at least three distinct precipitate phases arranged in a broken-up network; (d-e) high-magnification imaging of the interface between a Ce-rich precipitate and the Al matrix. In (e) the sample is oriented such that the atomic planes are visible for the Ce-rich precipitate but not the Al matrix. (f) shows EDS mapping performed on the entire region imaged in (d). Samples were taken from the grip region of a sample tested in tension at room temperature.

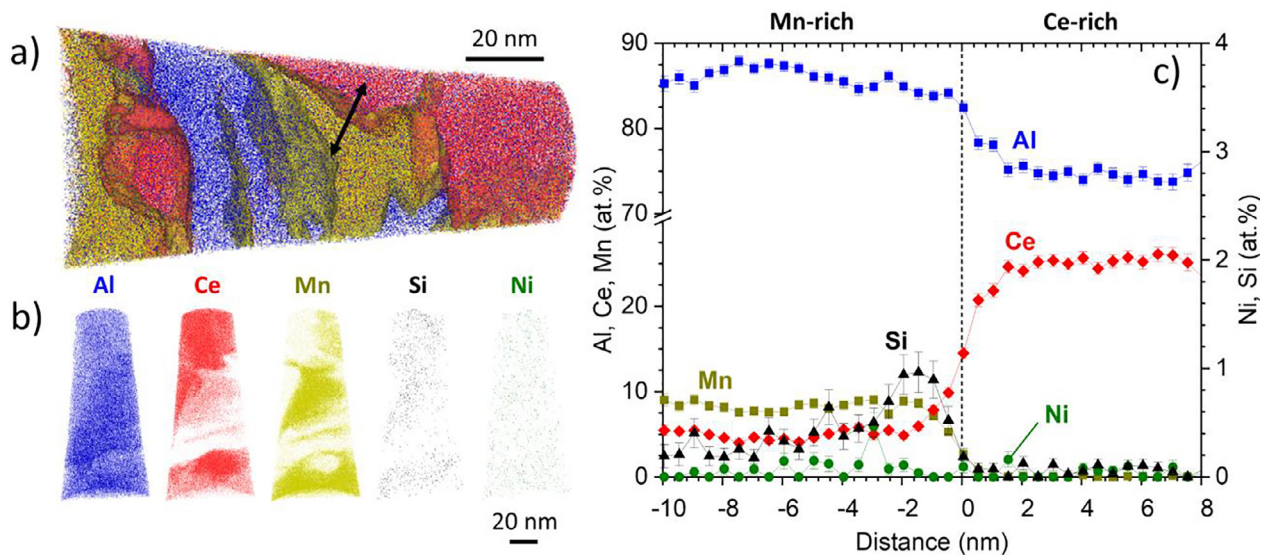


Fig. 3. APT analysis of as-SR AM Al-Ce-Ni-Mn: (a) 3-D reconstruction with individual atoms shown and 10 at.% Ce and 4 at.% Mn isoconcentration surfaces drawn in red and yellow, respectively; (b) 3-D atom maps showing the distribution of each individual atomic species; (c) a proximity histogram showing the elemental distributions across a Mn-rich precipitate/Ce-rich precipitate interface, as indicated by the black arrow in (a). An enrichment of Si is noted near the interface. Compositions of each phase as summarized in Table S1 are taken at the plateau regions of the elemental distribution curves (For interpretation of the references to color in this figure legend, the reader is referred to the web version of this article).

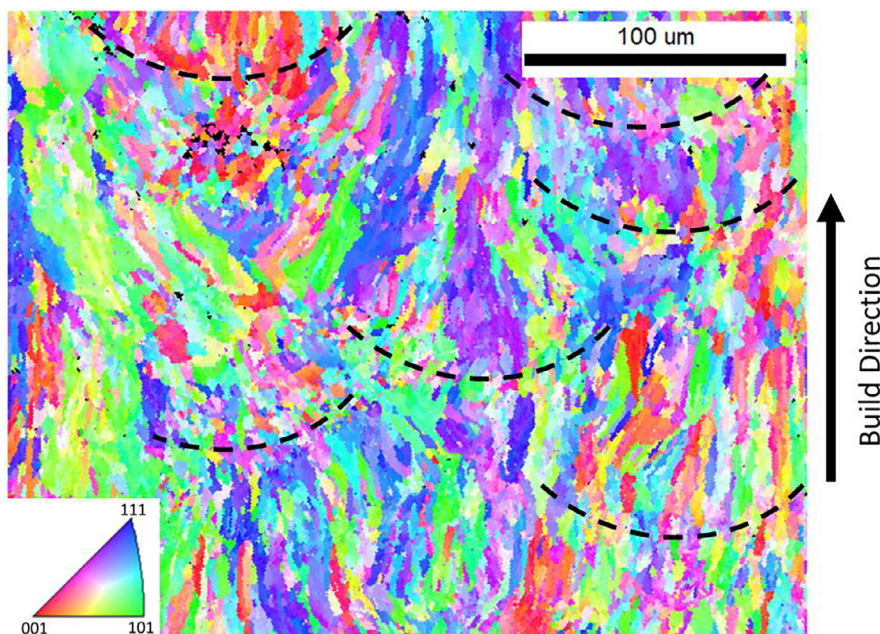


Fig. 4. Inverse pole figure map showing the grain structure of as-SR AM Al-Ce-Ni-Mn alloy as imaged using electron backscatter diffraction (EBSD), with orientations shown relative to the build direction. Several melt pool boundaries (MPBs) are highlighted with dashed lines.

appreciable levels in the matrix, with a matrix concentration of 0.10 ± 0.06 at.%. For the discussion of mechanical properties to follow, we note that the precise chemical compositions of the precipitate phases are not highlighted and that the intermetallic precipitates are incoherent with the matrix and too large to be sheared, which was confirmed by STEM investigations.

The structure of the Al grains in the as-SR material as analyzed using EBSD is shown in Fig. 4 and consists of primarily columnar grains on the order of $\sim 10 \mu\text{m}$ in width and $\sim 100 \mu\text{m}$ in length. There is no strong crystallographic texture, however the long axes of the columnar grains tend to be oriented along the build direction. The melt pool boundaries are visible and several are outlined with dashed lines. Small equiaxed grains are present at several of the melt pool boundaries, which likely prevented epitaxial grain

growth across the melt pools during solidification, contributing to the hot tear resistance of the alloy.

3.2. Ambient- and high-temperature mechanical properties

Tensile testing was conducted on as-SR samples at room temperature and several temperatures between 300 and 400 °C, with the load applied along the build direction. The measured yield strengths, ultimate tensile strengths, and elongations are plotted in Fig. 5a. The creep elongation values are also plotted for comparison and will be discussed in Sections 3.4 and 4.4. The yield and ultimate tensile strengths are maximum at room temperature, 258 ± 4 and 370 ± 4 MPa, respectively, and decrease with increasing temperature, while the elongation displays the opposite

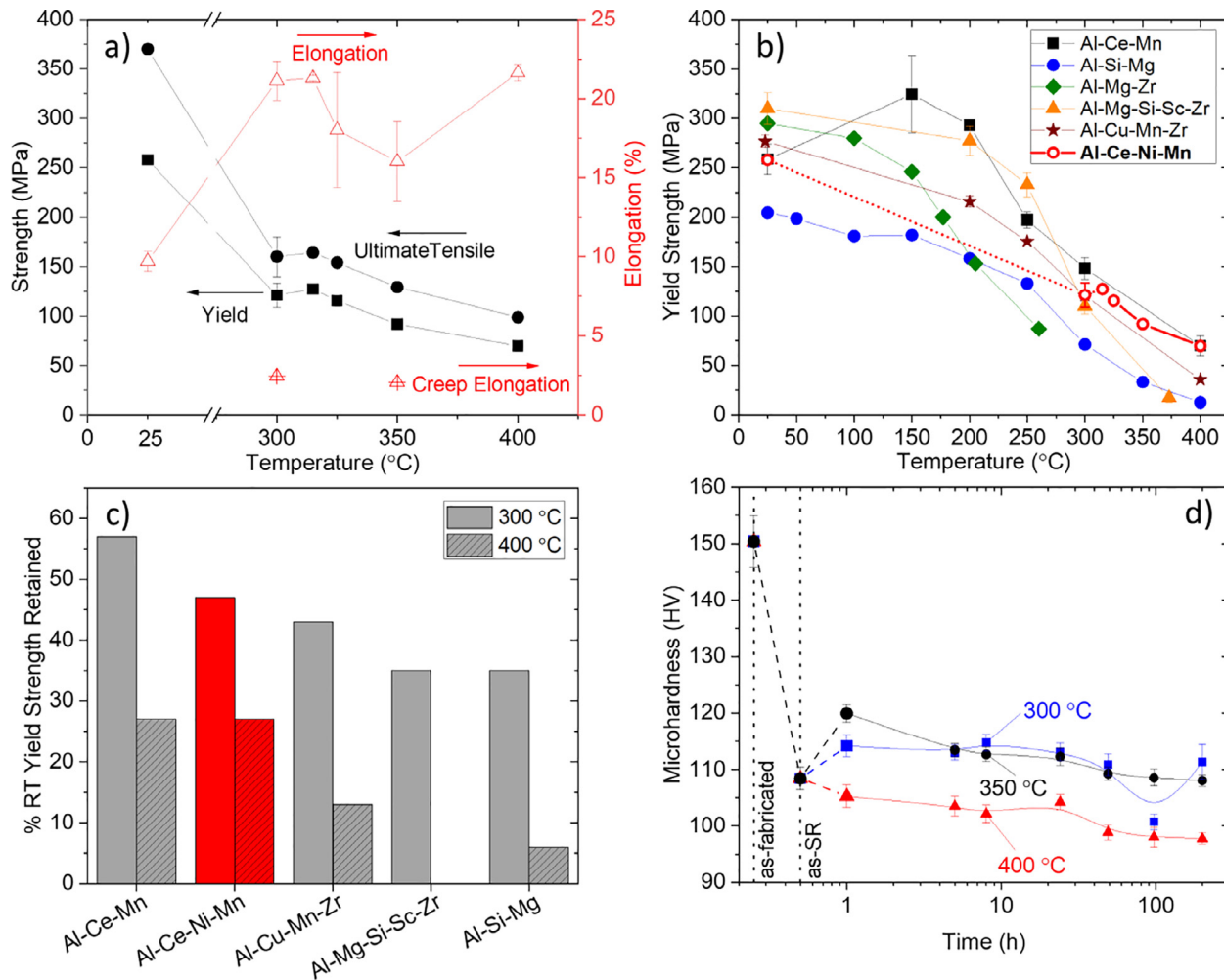


Fig. 5. (a) Yield strength, ultimate tensile strength, tensile elongation, and tensile creep elongation for as-SR AM Al-Ce-Ni-Mn as a function of temperature. Creep elongation is discussed in Sections 3.4 and 4.4; (b) yield strength of the present AM Al-Ce-Ni-Mn alloy compared with several other as-printed AM Al alloys as a function of temperature. Included for comparison are Al-10Ce-8Mn [16], Al-2.9Mg-2.1Zr [2], Al-14.1Mg-0.47Si-0.31Sc-0.17Zr [46], Al-8.6Cu-0.45Mn-0.90Zr [25], and Al-10Si-0.3Mg [4]; (c) percent retention of room-temperature (RT) tensile yield strength at 300 and 400 °C for the AM alloys in (b); (d) evolution of ambient-temperature Vickers microhardness of AM Al-Ce-Ni-Mn after aging at 300, 350 and 400 °C for up to 200 h.

trend. The room-temperature ductility of $10 \pm 1\%$ is appreciable considering the high volume fraction ($\sim 35\%$) of potentially brittle intermetallics in the alloy. The tensile properties in the intermediate temperature range of $100\text{--}300\text{ }^{\circ}\text{C}$ were also evaluated, since several high-temperature Al alloys such as Al-Fe-V-Si and Al-Cr-Zr produced by the powder metallurgy (PM) route have exhibited ductility minima in this temperature range [44,45]. Details are given in the supplementary information. For the present AM Al-Ce-Ni-Mn alloy, no significant ductility drop is noted within the $100\text{--}300\text{ }^{\circ}\text{C}$ temperature range, Fig. S2. In the PM alloys, the decrease in ductility was attributed to dynamic strain aging (DSA) from solute elements such as Fe, V, and Cr in the matrix which become mobile at elevated temperatures. The nearly pure Al matrix in the present AM Al-Ce-Ni-Mn alloy, Table S1, may therefore contribute to the lack of an observed DSA effect at $100\text{--}300\text{ }^{\circ}\text{C}$.

When compared to other AM aluminum alloys tested at high temperatures, Fig. 5b, the present Al-Ce-Ni-Mn alloy displays modest yield strength at $T \leq 300\text{ }^{\circ}\text{C}$, but at $T > 300\text{ }^{\circ}\text{C}$ the strength is greater than several of the alloys. For example, at $400\text{ }^{\circ}\text{C}$ the yield strength is 57 MPa higher (~ 6 times higher) than AM Al-10Si-0.3Mg [4] and is the same as a recently reported Al-Ce-Mn alloy [16]. Furthermore, the percentage of room-temperature strength retained, 47% at $300\text{ }^{\circ}\text{C}$ and 27% at $400\text{ }^{\circ}\text{C}$, is also higher than that

for Al-Si-Mg (35% at $300\text{ }^{\circ}\text{C}$ and 6% at $400\text{ }^{\circ}\text{C}$), Al-Mg-Si-Sc-Zr (35% at $300\text{ }^{\circ}\text{C}$), and Al-Cu-Mn-Zr (43% at $300\text{ }^{\circ}\text{C}$ and 13% at $400\text{ }^{\circ}\text{C}$), but slightly less than that of Al-Ce-Mn (57% at $300\text{ }^{\circ}\text{C}$ and 27% at $400\text{ }^{\circ}\text{C}$, Fig. 5c).

The evolution of strength as a function of aging time at 300, 350 and $400\text{ }^{\circ}\text{C}$ was evaluated using microhardness measurements, with results shown in Fig. 5d. The stress-relief heat treatment decreases the microhardness significantly from 150 to 108 HV, but during further aging at $300\text{--}400\text{ }^{\circ}\text{C}$, the microhardness remains relatively stable up to 200 h. The microhardness plateaus at ~ 110 HV during aging at $300\text{--}350\text{ }^{\circ}\text{C}$ and exhibits a slight downward trend overall at $400\text{ }^{\circ}\text{C}$, falling to 98 HV after 200 h.

3.3. Creep behavior

The as-SR AM Al-Ce-Ni-Mn alloy was creep tested in tension between 300 and $400\text{ }^{\circ}\text{C}$, with plots of minimum strain rate vs. stress shown in Fig. 6a. The alloy appears to undergo power-law creep according to the equation [47]:

$$\dot{\varepsilon} = A\sigma^{n_{app}} \exp\left(-\frac{Q_{app}}{R_g T}\right) \quad (1)$$

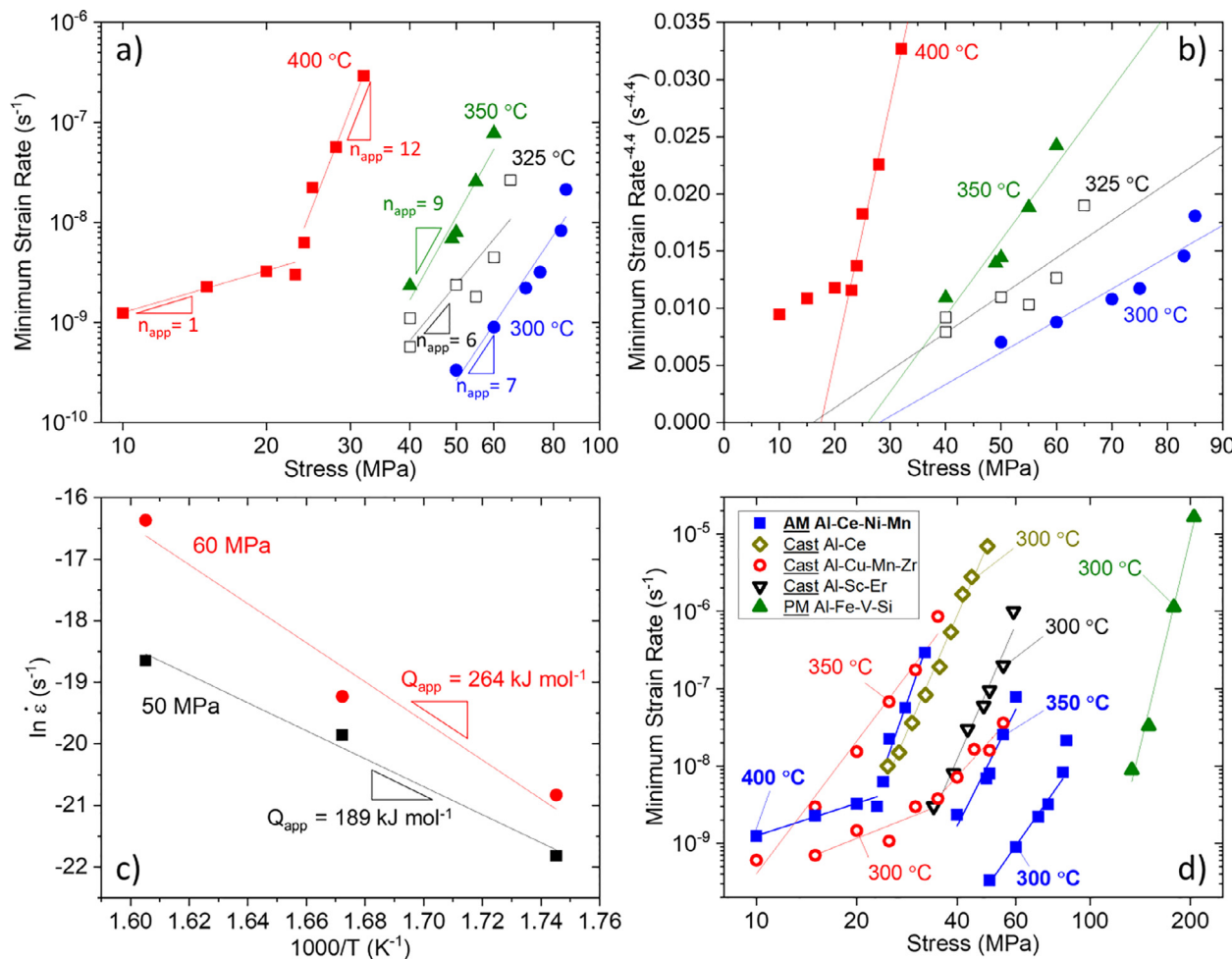


Fig. 6. (a) Minimum strain rate vs. stress at 300–400 °C for the as-SR AM Al-10.5Ce-3.1Ni-1.2Mn alloy with apparent stress exponents n_{app} for diffusional and dislocation creep shown; (b) Plots of $\dot{\varepsilon}^{1/n}$ vs. σ with $n = 4.4$ for pure Al to determine the threshold stress for creep of AM Al-Ce-Ni-Mn at each test temperature. The points of intersection with the x-axis are the threshold stress values σ_{th} ; (c) Arrhenius plot showing apparent creep activation energies measured at 50 and 60 MPa. The slopes are equal to $-Q_{app}/R_g$; (d) Creep behavior of the present AM Al-Ce-Ni-Mn alloy compared with cast and powder metallurgy (PM) alloys from the literature: Al-12.5Ce [50], Al-6.4Cu-0.19Mn-0.13Zr [51], Al-0.10Sc-0.12Er [52], and Al-8.5Fe-1.3V-1.7Si [53]. All alloys were tested in tension, except for Al-0.10Sc-0.12Er and Al-12.5Ce which were tested in compression.

Table 3

Summary of n_{app} and threshold stresses σ_{th} measured for the AM Al-Ce-Ni-Mn alloy under tensile creep at 300–400 °C.

Temperature (°C)	Diffusional Creep n_{app}	Dislocation Creep n_{app}	σ_{th} (MPa)
300	-	7	28
325	-	6	16
350	-	9	26
400	1	12	18

where $\dot{\varepsilon}$ is the minimum strain rate, σ is the applied stress, A is a dimensionless material constant, Q_{app} is the apparent creep activation energy, n_{app} is the apparent stress exponent, R_g is the ideal gas constant, and T is the absolute temperature. Fits to Eq. (1) are plotted as the solid lines in Fig. 6a for each test temperature and values of n_{app} are summarized in Table 3. Dislocation creep regimes, evidenced by values of n_{app} ranging from 6 to 12, are present for each test temperature. At 400 °C a diffusional creep regime is observed at low stresses, indicated by $n_{app} = 1$. Compared to $n_{app} = 4.4$ expected for dislocation creep in pure Al [48], the values of n_{app} measured here for dislocation creep in AM Al-Ce-Ni-Mn are higher, indicative of a threshold stress. The threshold stress σ_{th} below which creep deformation cannot macroscopically

be measured may be incorporated in the power-law creep equation [49]:

$$\dot{\varepsilon} = A'(\sigma - \sigma_{th})^n \exp\left(-\frac{Q}{R_g T}\right) \quad (2)$$

where A' is a dimensionless material constant, n is the matrix stress exponent, and Q is the matrix activation energy for dislocation climb. The threshold stresses for dislocation creep are thus determined by plotting $\dot{\varepsilon}^{1/n}$ vs. σ with $n = 4.4$ and extrapolating to $\dot{\varepsilon} = 0$ using a weighted least squares linear regression, as shown in Fig. 6b. A summary of the obtained values for σ_{th} are also listed in Table 3. The value of Q_{app} can be calculated from Eq. (1) using minimum strain rates measured at the same stress but different temperatures:

$$Q_{app} = -R_g \frac{d \ln \dot{\varepsilon}}{d(\frac{1}{T})} \quad (3)$$

Fig. 6c shows an Arrhenius plot using minimum strain rates measured at 50 and 60 MPa and temperatures of 300, 325 and 350 °C, where the slopes of the curves are equal to $-Q_{app}/R_g$. The measured values of Q_{app} ranging from 189 to 264 kJ mol⁻¹ are also consistent with the presence of a threshold stress, as they are greater than the value of 142 kJ mol⁻¹ for vacancy diffusion (and thus the activation energy for dislocation climb) in pure Al [48].

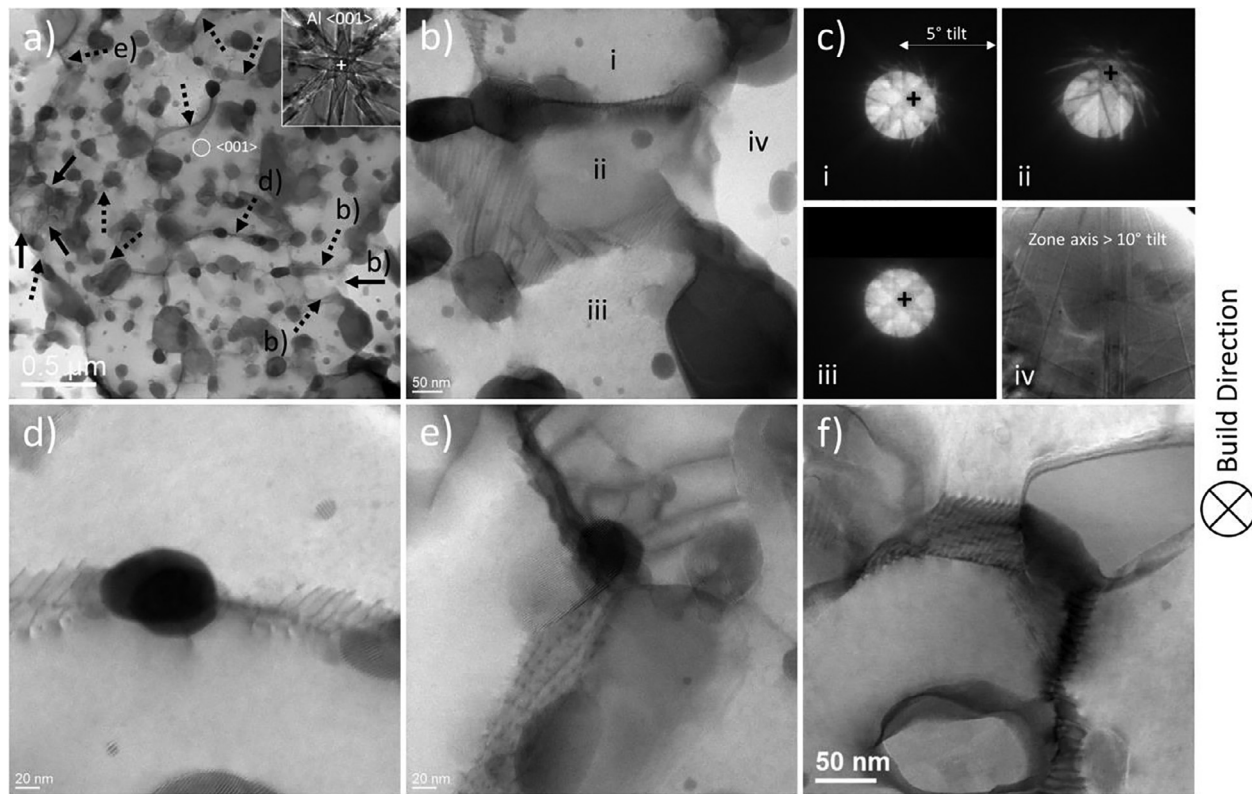


Fig. 7. Bright-field STEM images of as-SR AM Al-Ce-Ni-Mn crept to fracture at 300 °C for 433 h under a single applied tensile stress of 83 MPa: (a) representative subgrain boundary network, with region circled in white oriented to the Al <001> zone axis. Corresponding Kikuchi pattern is shown in the inset. Dotted arrows indicate analyzed low-angle boundaries and solid arrows indicate high-angle boundaries; (b) Detail of area with subgrains (regions i–iii) and an adjacent grain (region iv); (c) Kikuchi patterns from regions in (b) showing < 5° tilt between subgrains and > 10° relative to the neighboring grain. The distance from the center to the edges of the Kikuchi maps corresponds to 5° tilt. The black crosses show the location of the Al <001> zone axis for each region; (d–f) detail of dislocation networks comprising the subgrain boundaries. (d–e) show detail of regions from (a), while (f) shows an additional region aligned close to the Al <110> zone axis. Sample was extracted from the gauge section of the tensile creep specimen.

When compared to cast Al alloys with high creep resistance and microstructural thermal stability such as Al-12.5Ce [50], Al-6.4Cu-0.19Mn-0.13Zr [51], and Al-0.10Sc-0.12Er [52], Fig. 6d, the as-SR AM Al-10.5Ce-3.1Ni-1.2Mn alloy performs remarkably well. The creep resistance of the present AM alloy at 350 °C is superior to that of cast Al-Cu-Mn-Zr and Al-Sc-Er at 300 °C. The increase in high-temperature performance of the present AM alloy extends to 400 °C, where the AM Al-Ce-Ni-Mn creep resistance is comparable to that of Al-Cu-Mn-Zr at 350 °C and Al-Ce at 300 °C. On the other hand, the creep strength of the present AM alloy at a given minimum creep rate is approximately 40–50% lower than that of an Al-8.5Fe-1.3V-1.7Si alloy produced by a rapid solidification and powder metallurgy (PM) route [53]. At 300 °C, the PM Al-Fe-V-Si exhibits a threshold stress near ~100 MPa, about four times greater than that of AM Al-Ce-Ni-Mn at the same temperature.

STEM imaging was performed on a sample crept to fracture at 300 °C for 433 h under a single applied tensile stress of 83 MPa, with results shown in Fig. 7. Micron-scale subgrains are present, with subgrain boundaries consisting of dislocation networks extending between the intermetallic phases. The intermetallic particles act as subgrain boundary junctions and appear to restrict migration of the dislocation networks. Some high-angle grain boundaries are also present. Fig. 7b shows detail of a region containing several subgrain boundaries and a high-angle grain boundary. There is < 5° tilt between each subgrain (regions i–iii) as shown by Kikuchi patterns captured in Fig. 7c, while the tilt relative to the neighboring grain (region iv) is > 10°. Detail of several different subgrain boundaries is shown in Figs. d–f, revealing the dislocation networks comprising the boundaries. Fig. S3 in the supple-

mental information demonstrates that the degree of tilt between subgrains as measured by the Kikuchi patterns is consistent with the observed dislocation spacings, and that tilting of the sample changes the subgrain boundary contrast as diffraction conditions controlling dislocation visibility change.

3.4. Fracture

The fracture surfaces observed after tensile loading under several different conditions are shown in Fig. 8. The characteristics of the fracture surfaces change significantly depending on temperature and type of test. For the 25 °C tensile test (Fig. 8a), the fracture surface clearly shows remnants of the laser tracks from AM processing, i.e., the elongated semicircular grooves with widths of ~100–200 μm. The laser track remnants indicate preferential fracture along the MPBs. Fine dimpling at higher magnifications (Fig. 8b) suggests that ductile fracture is dominant at room temperature. Thus, ductile fracture propagates along the MPBs during tensile testing at 25 °C. The resulting ductility of the alloy under these conditions is a moderate 10%. When the tensile test temperature is raised to 300 °C, the ductility increases significantly to 21% and the fracture surface shows relatively coarse dimpling (Fig. 8c,d) characteristic of ductile fracture. The laser track remnants are no longer evident, suggesting that fracture does not preferentially take place along the MPBs. Under creep loading conditions, the fracture surface is stepped, with several flat plateau regions (Fig. 8e). Higher magnifications reveal a mixed fracture surface (Fig. 8f), with dimpled regions characteristic of ductile fracture between the flat plateau regions. Given the prevalence of the flat plateau regions,

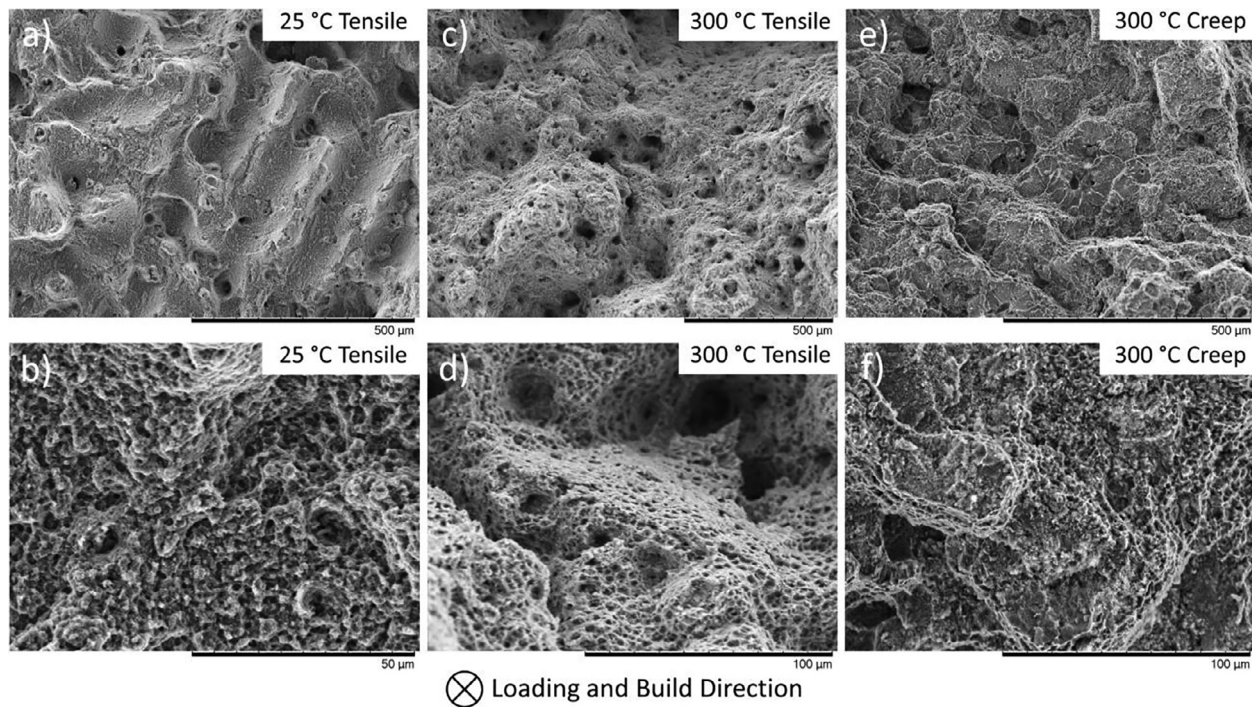


Fig. 8. Fracture surfaces of as-SR AM Al-Ce-Ni-Mn observed after (a–b) tensile testing at room temperature, (b–c) tensile testing at 300 °C, and (e–f) creep testing at 300 °C. In (e–f) the specimen was crept for 433 h at a single applied stress of 83 MPa.

they likely are responsible for the relatively low elongation at fracture of 2.5% under creep loading conditions at 300 °C. For a given test type in the temperature range of 300–400 °C, the overall character of the fracture surface (ductile, plateau regions, or mixed) does not change with test temperature as shown in Fig. S4 of the supplemental information.

3.5. Microstructural Evolution

The evolution of the microstructure after isothermally aging at 300, 350, and 400 °C for 200 h is shown in Fig. 9a–c, with corresponding measurements of precipitate radius as a function of the expected two-dimensional diffusion distance of Mn—calculated based on the time and temperature of the aging treatment—shown in Fig. 9d. The expression $x = \sqrt{4Dt}$ was used to calculate the expected diffusion distances of Mn, where x is the mean diffusion distance, D is the diffusivity of Mn in pure Al [54], and t is the diffusion time. For comparison with the as-SR microstructure, see Fig. 1b. Also shown in Fig. 9d are measurements of precipitate radius after creep testing at various times and temperatures as a function of Mn diffusion distance. Corresponding representative post-creep microstructures are shown in Fig. S5 of the supplemental information. For post-creep microstructural evaluation, samples from the gauge sections of crept specimens were utilized.

Under load-free conditions the precipitate size is stable up to at least 350 °C for 200 h, with no measurable change relative to the as-SR precipitate radius of 118 ± 29 nm. After 200 h at 400 °C the average precipitate radius increases 17% to 138 ± 8 nm. Under creep loading conditions precipitate coarsening is enhanced, with the precipitate radius increasing to 162 ± 21 after creep testing at 350 °C and further increasing to 215 ± 55 nm after creep testing at 400 °C, increases of 37 and 82% relative to the as-SR state, respectively. The volume fraction of precipitates remains relatively stable at ~35% during load-free and creep loading conditions at 300–400 °C as shown in Fig. S5d.

4. Discussion

4.1. Microstructural coarsening

The microstructure of AM Al-Ce-Ni-Mn in the as-SR state is remarkably coarsening-resistant upon aging at elevated temperatures, as evidenced by only a 17% increase in average precipitate radius after 200 h of load-free annealing at 400 °C, Fig. 9d. The stability of the measured microhardness values after stress-relief, Fig. 5d, further supports this conclusion. Note that in the following discussion of microstructural coarsening, we measure and report only the average precipitate size, which includes all the precipitate types listed in Table S1. The coarsening rates of individual phases may be different and proportions of the various phases present in the alloy may change with time, but these measurements are beyond the scope of the present study. Furthermore, since the strengthening and creep mechanisms we will use to describe the behavior of the alloy relate only to the average precipitate radius, the characteristics of the individual precipitates are not discussed.

The excellent coarsening resistance of the microstructure is likely related to both the low solubilities and low diffusivities of the major solute elements Ce, Ni, and Mn in the Al matrix. For coarsening to occur, solutes must diffuse through the matrix from small precipitates to large precipitates. A low solute solubility in the matrix is therefore a thermodynamic barrier to coarsening while a low solute diffusivity is a kinetic barrier. Fig. S6 in the supplemental information shows a plot of maximum solute solid solubilities in Al and solute diffusivities in Al at 400 °C. Also plotted are several relevant solutes related to various literature alloys discussed in this paper. Although the diffusivity of Ni in Al at 400 °C is similar to self-diffusion of Al ($\sim 10^{-15} \text{ m}^2 \text{ s}^{-1}$), its low solubility in Al of ~0.02 at.% provides a thermodynamic barrier to coarsening. Consequently, in cast Al-Ni alloys the strengthening Al_3Ni microfibers are coarsening-resistant to ~400 °C [55–58]. Cerium has even lower solubility in Al of < 0.01 at.%, and its diffusivity in Al is

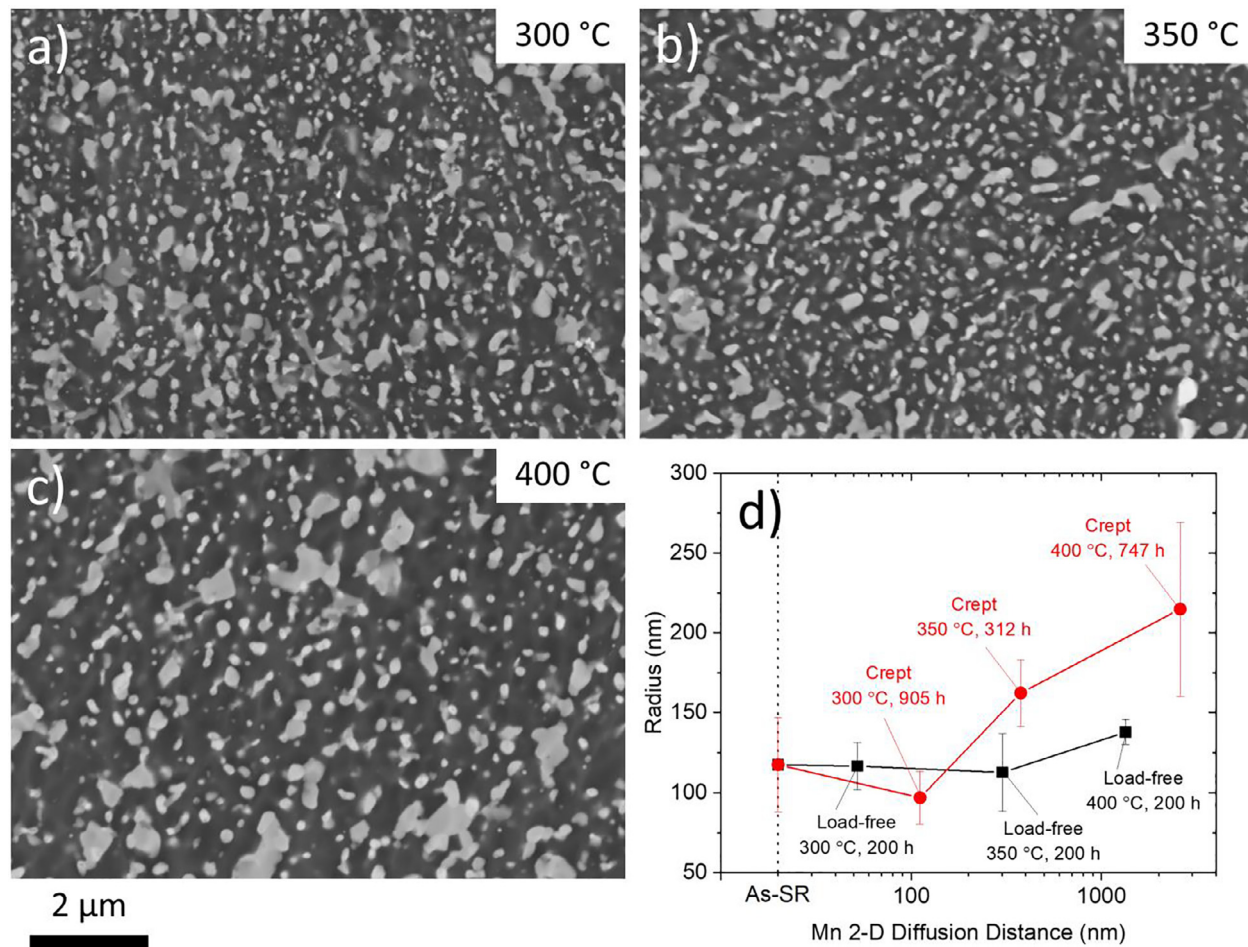


Fig. 9. (a–c) SEM-BSE micrographs showing evolution of the AM Al-Ce-Ni-Mn microstructure after load-free annealing for 200 h at 300–400 °C. For the as-SR microstructure, see Fig. 1b. Coarsening of precipitate phases is evident only at 400 °C; (d) plot of measured average precipitate radius as a function of expected two-dimensional diffusion distance of Mn, calculated based on the aging/creep time and temperature, and diffusivity value in Ref. [54]. For creep loading at 300 °C, measurements were taken on a sample tested under a maximum load of 85 MPa. At 350 °C measurements were taken on a sample tested under a maximum load of 60 MPa. At 400 °C measurements were taken on a sample tested under a maximum load of 32 MPa.

~four orders of magnitude lower than Ni. As a result, in cast Al-Ce alloys, $\text{Al}_{11}\text{Ce}_3$ strengthening precipitates are coarsening-resistant for hundreds of hours at $T \geq 400$ °C [50,59,60]. Manganese has a similar diffusivity in Al as Ce, but higher solubility (0.6 at.%). It is therefore not surprising that the strengthening phases in the present alloy, which are comprised largely of Ce, Ni, and Mn, are resistant to coarsening.

Under creep loading the coarsening of precipitates increases and becomes measurable at $T \geq 350$ °C, as shown in Fig. 9d. For a given expected diffusion distance of Mn—the slowest diffusing solute in the AM Al-Ce-Ni-Mn alloy—the measured precipitate radii under creep loading conditions are larger, suggesting enhanced solute diffusion. This observation agrees with a previous study on a rapidly solidified and consolidated Al-8.8Fe-3.7Ce alloy, i.e., a distribution of submicron diameter incoherent precipitates ($\text{Al}_{13}\text{Fe}_4$ and $\text{Al}_{10}\text{Fe}_2\text{Ce}$) at a volume fraction of ~22% [61]. In that study, the authors attributed enhanced coarsening of precipitates under creep loading at 17.2 MPa and 425 °C to the generation of excess vacancies along grain boundaries by plastic deformation and enhanced diffusion of solutes between precipitates, facilitated by pipe diffusion along dislocations connecting the precipitates. Since the grain size in the present AM Al-Ce-Ni-Mn alloy (~10–100 μm) is orders of magnitude greater than that reported for the Al-Ce-Fe alloy (~0.9 μm), the effect of grain boundary diffusion on coarsen-

ing in AM Al-Ce-Ni-Mn is likely small. Thus, the enhanced coarsening under creep is expected to be from solute pipe diffusion along the dislocation network formed during creep. Like bulk diffusivity, the pipe diffusivity increases exponentially with temperature [61], in agreement with the observation of increased coarsening at higher temperatures.

The coarsening-resistance of the AM Al-Ce-Ni-Mn is the as-SR state highlights the potential benefits of annealing what would traditionally be considered a non-heat treatable alloy at a temperature higher than the intended service temperature. In this case the stress-relief anneal is 50 °C higher than the highest test temperature of 400 °C. There is a tradeoff in strength, evidenced by the 42 HV decrease in microhardness between the as-fabricated and as-SR state, but the stress-relief treatment clearly stabilizes the microstructure such that it does not dramatically change during additional aging at 300–400 °C. This heat treatment design strategy may therefore be useful for long-lifetime components that operate in the 300–400 °C temperature range.

4.2. Strengthening mechanisms

Strengthening in the AM Al-Ce-Ni-Mn alloy can be modeled as a superposition of several different mechanisms, including solid solution strengthening, grain boundary strengthening, Orowan dislocation looping, and load transfer. The increment of strengthening

due to solid solution strengthening, $\Delta\sigma_{SS}$, will be determined by Mn, as it is the only solute in the matrix at an appreciable concentration, Table S1. The increment in strength is [62]:

$$\Delta\sigma_{SS} = AC_{Mn}\beta \quad (4)$$

where $A = 54.8$ at.%⁻¹ and $\beta = 1$ are empirically derived constants for Mn in Al [62] and C_{Mn} is the matrix concentration of Mn in at.%. Using the matrix Mn concentration of 0.1 ± 0.06 at.% as measured by APT in the as-SR state, the expected $\Delta\sigma_{SS}$ is small at 5 ± 3 MPa.

The increment in strength from grain boundaries, $\Delta\sigma_{H-P}$, is given by the classic Hall-Petch relationship [63]:

$$\Delta\sigma_{H-P} = \frac{k_{H-P}}{\sqrt{d}} \quad (5)$$

where $k_{H-P} = 90$ MPa $\sqrt{\mu m}$ is an empirically derived constant [63] and d is the average grain diameter. Since most grains in the alloy are not equiaxed, we assume an average grain diameter of $10-100 \mu\text{m}$. Using these values of d , the increment in strength due to grain boundaries is 19 ± 10 MPa.

The increment in strength provided Orowan dislocation looping around non-shearable precipitates, $\Delta\sigma_{Or}$ is given as [64]:

$$\Delta\sigma_{Or} = M \frac{0.4}{\pi} \frac{Gb}{\sqrt{1-\nu}} \ln \left[\frac{2(\sqrt{\frac{2}{3}}\langle R \rangle)}{b} \right] \quad (6)$$

where $M = 3.06$ is the mean matrix orientation factor for Al [65], $b = 0.286$ nm is the magnitude of the matrix Burgers vector in Al [48], $\nu = 0.345$ is the Poisson's ratio for Al [65], $G = 25.4$ GPa is the shear modulus of pure Al [48], and $\langle R \rangle$ is the average precipitate radius. The edge-to-edge interprecipitate distance λ is calculated from $\langle R \rangle$ and the precipitate volume fraction ϕ , assuming a homogenous distribution of spherical precipitates on a cubic grid [66]:

$$\lambda = \left[\left(\frac{3\pi}{4\phi} \right)^{1/2} - 1.64 \right] \langle R \rangle \quad (7)$$

Using $\langle R \rangle = 118 \pm 29$ nm as measured in the as-SR state and the precipitate volume fraction of 35%, the strength from Orowan looping around the precipitates is 213 ± 45 MPa.

Summing all the strengthening increments discussed thus far and accounting for the yield strength of pure Al, 27 MPa [67], an ambient-temperature yield strength of 264 ± 58 MPa is predicted in the as-SR state, in excellent agreement with the experimentally measured yield stress of 258 ± 4 MPa. Although the agreement between the modeled and measured yield stress is encouraging, load transfer is also expected to play a role in strengthening of the AM Al-Ce-Ni-Mn alloy, as its high precipitate volume fraction suggests it should be treated as a composite. Analysis of the creep behavior in Section 4.5 also demonstrates that treatment as a composite is necessary. The effective stress on the matrix σ_{eff} resulting from load transfer provided by a reinforcing phase was derived by Hong and Chung [68] from the shear-lag model of Nardone and Prewo [69] for strengthening of Al-SiC composites:

$$\sigma_{eff} = \sigma\alpha_{LT} = \sigma \left[1 - \frac{\phi \left(\frac{s}{2} + 1 \right)}{\phi \left(\frac{s}{2} + 1 \right) + (1 - \phi)} \right] \quad (8)$$

where s is the aspect ratio of the reinforcement and α_{LT} is the load transfer coefficient. Using $\phi = 0.35$ and $s = 1$ for the AM Al-Ce-Ni-Mn alloy, a value of 0.55 is calculated for α_{LT} , suggesting that load transfer plays a significant role in strengthening, as nearly half of the applied load is transferred to the precipitate phase. An estimate for the yield stress increment due to load transfer, $\Delta\sigma_{LT}$, is given by the shear-lag theory of Nardone and Prewo [69]:

$$\Delta\sigma_{LT} = 1/2\sigma_m V_f(s+2) \quad (9)$$

where σ_m is the yield stress of the matrix material without reinforcement. However, Eq. (9) often underestimates the yield strength of composites with a low-strength matrix, such as the present AM Al-Ce-Ni-Mn where the matrix is essentially pure Al [70]. The value of matrix yield strength may be corrected by including strengthening from thermal expansion dislocations, subgrains, geometrically necessary dislocations, etc., but for an upper estimate of $\Delta\sigma_{LT}$ the value of the matrix/reinforcement interface strength σ_{int} may be used in place of σ_m . Assuming the precipitate/ matrix interfaces in the present alloy have similar strengths to that of the Al/SiC interface (133 MPa [71]), a maximum value of 70 MPa is obtained for $\Delta\sigma_{LT}$. Using instead $\sigma_m = 27$ MPa [67] for the yield of a pure Al matrix in Eq. (9), a minimum value for $\Delta\sigma_{LT}$ of 14 MPa is obtained. Given that this range of $\Delta\sigma_{LT}$ values (14–70 MPa) is comparable to the uncertainty in $\Delta\sigma_{Or}$ (± 45 MPa), which accounts for ~80% of the yield strength, we may reasonably consider strengthening from load transfer to be active in the AM Al-Ce-Ni-Mn alloy in addition to solid solution, grain boundary, and particle strengthening.

4.3. Tensile behavior

Compared to the other alloys shown in Fig. 5b, the AM Al-Ce-Ni-Mn alloy has modest yield strength at room temperature but displays an improved retention of yield strength at elevated temperatures. The reduced room-temperature yield strength compared to AM Al-2.9Mg-2.1Zr [2] and AM Al-14.1Mg-0.47Si-0.31Sc-0.17Zr [46] is likely due to the lack of Mg solid-solution strengthening. According to first principles calculations [72], 2.9% and 14.1 wt.% Mg are expected to provide 54 and 154 MPa of solid solution strengthening, respectively. In addition, the Zr/Sc content of the latter alloys promotes regions of refined grains with diameters of $\sim 1 \mu\text{m}$ or less from solidification of primary $\text{Al}_3(\text{Zr},\text{Sc})$ particles, contributing to enhanced grain boundary strengthening compared to the $10-100 \mu\text{m}$ grains of the present alloy. The room-temperature strength of AM Al-Ce-Ni-Mn is instead comparable to the AM Al-10Ce-8Mn [16] and AM Al-8.6Cu-0.45Mn-0.90Zr [25] alloys, which are also strengthened by dispersions of intermetallic phases.

Performance benefits of the AM Al-Ce-Ni-Mn alloy are revealed during tensile testing at high temperatures. Whereas the strengthening phases in other alloys such as such as Mg_2Si in Al-Mg-Si-Sc-Zr [46], $\theta\text{-Al}_2\text{Cu}$ in Al-Cu-Mn-Zr [25], and the Si eutectic network in Al-Si-Mg [4] coarsen rapidly at elevated temperatures and contribute to reduced strengths, the coarsening resistance of the AM Al-Ce-Ni-Mn alloy, Fig. 9, allows it to maintain higher yield strengths at $T > 300^\circ\text{C}$. Furthermore, as we will discuss in the next section, grain boundary sliding during creep deformation appears to be suppressed in AM Al-Ce-Ni-Mn for $T \leq 350^\circ\text{C}$. This observation during creep suggests that grain boundary sliding, which contributes significantly to the reduction in yield strength of Al-2.9Mg-2.1Zr [2] at elevated temperatures, may also be suppressed during tensile deformation of AM Al-Ce-Ni-Mn.

4.4. Creep ductility

Despite its excellent overall creep resistance, the as-SR AM Al-Ce-Ni-Mn alloy suffers from low creep ductility of $\sim 2\%$ compared to 10% during ambient-temperature tensile tests and $\sim 20\%$ during elevated-temperature tensile tests. An examination of the creep specimens reveals that voids appear to preferentially form at the MPBs within the gauge section, Fig. 10. Based on this observation and prior studies of fracture in AM Al-Si-Mg and Al-Cu-Ce alloys, we propose that the limited ductility measured during creep is primarily due to preferential void formation and growth along the MPBs.

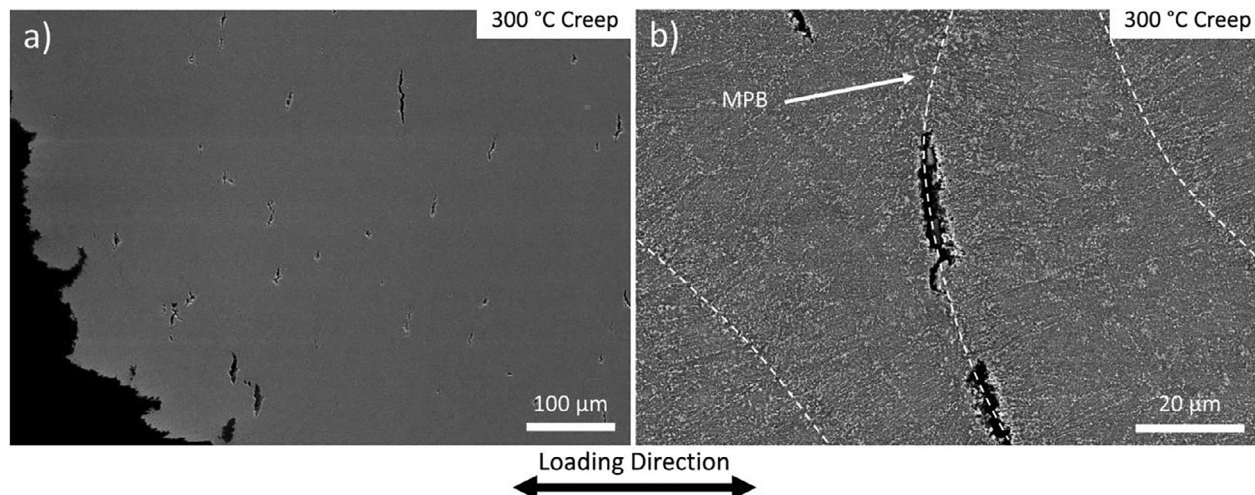


Fig. 10. Fractured creep sample tested at 300 °C for 905 h at a maximum stress of 85 MPa, imaged along the gauge section. The low magnification image (a) shows several voids that formed in the bulk material away from the fracture surface at the far left. The representative high magnification image (b) shows a void which preferentially formed along an MPB.

In AM Al-Si-Mg alloys, fracture during ambient-temperature mechanical testing occurs preferentially along the MPBs [73–75]. Within the MPB region is a heat affected zone (HAZ) in which the continuous and interconnected Si eutectic network that forms upon printing is broken up and spheroidized from heating occurring during subsequent laser passes and material re-melting. Delahaye et al. [73] proposed that spheroidization of the Si eutectic creates a locally weak region prone to strain localization, dislocation pileup, and void formation during plastic deformation, decreasing the ductility of AM components. Similarly, strain localization was observed in the HAZ of an AM Al-9Cu-6Ce alloy, leading to preferential fracture along the HAZ and a dip in ductility during tensile testing at 300 °C [76].

Since the MPB structure of the AM Al-Ce-Ni-Mn alloy is like that of AM Al-Si-Mg and AM Al-Cu-Ce, with a lower number density of coarser precipitates relative to the surrounding material, Fig. 1, similar strain localization is expected to occur. We therefore propose an inter-MPB creep fracture mechanism based on this hypothesis. During creep deformation of AM Al-Ce-Ni-Mn, dislocation pileup in the weaker MPB regions promotes void nucleation. Under high temperatures and normal stress, the voids grow by diffusional processes along the MPBs, eventually leading to their coalescence. When enough voids on MPBs coalesce, the effective stress applied to the material is high enough that the MPB fractures rapidly in a ductile manner between the coalesced MPB voids. Indeed, Fig. 10 shows several such voids at the MPBs with varying degrees of coalescence. This theory is also consistent with the creep fracture surfaces shown in Fig. 8e–f. The plateau-like regions are the MPB voids which have coalesced, with ductile fracture occurring between the plateau regions. Creep tests performed with the loading axis perpendicular to the build direction may be performed to further support the creep fracture mechanism and will be considered in future work. Under loading perpendicular to the build direction, void nucleation and growth will likely be reduced, allowing for higher creep elongations.

This scenario is also consistent with the fracture surfaces observed during ambient- and high-temperature tensile tests, which are completed in < 1 h and at strain rates (10^{-4} – 10^{-3} s $^{-1}$) that are orders of magnitude higher than creep deformation. During ambient-temperature tests, microvoids form preferentially along the MPBs due to strain localization. The microvoids cannot grow by diffusional processes at room temperature, therefore fracture occurs by microvoid coalescence driven by plastic deformation,

leaving behind clear laser track traces, Fig. 8a–b. High temperatures and strain rates during the elevated-temperature tensile tests lead to reduced strain localization, therefore microvoids nucleate throughout the material. The microvoids grow slightly before coalescing to create a ductile fracture, as evidenced by the larger microvoids in Fig. 8d compared to 8b. Since the voids nucleate throughout the material, the MPB structure is not evident on the fracture surface of the elevated-temperature tensile test specimen.

4.5. Creep deformation mechanisms

The detachment model of Arzt and Rösler (AR) [77,78] and constant structure model of Sherby, Klundt, and Miller (SKM) [79] have been alternately used to describe the creep behavior of dispersion strengthened aluminum alloys with similar microstructures to the present AM Al-Ce-Ni-Mn alloy, i.e., those with a high volume fraction of submicron intermetallic particles, such as in the Al-Fe-V-Si [80–83], Al-Fe-Ni [84,85], and Al-Fe-Ce [77,86] systems. Both models are considered for describing the creep behavior of the present AM Al-Ce-Ni-Mn alloy.

4.5.1. AR detachment model

In the AR detachment model [77,78], the creep rate is dependent on the thermally activated detachment of dislocations from strengthening particles as the dislocations bypass the particles by climb. The dislocations become pinned at the departure side due to an attractive dislocation/particle interaction from relaxation of the dislocation line tension at the incoherent particle/matrix interface. The degree of pinning is related to the parameter k , called the relaxation factor, which is the ratio of dislocation line energies at the particle/matrix interface and in the bulk. The creep equation is given as:

$$\dot{\varepsilon} = \frac{6\lambda_{AR}\rho D_L}{b} \cdot \exp\left(-\frac{Gb^2\langle R \rangle [(1-k) \cdot (1 - \sigma/\sigma_d)]^{3/2}}{k_b T}\right) \quad (10)$$

where λ_{AR} is $\frac{1}{2}$ the interprecipitate spacing λ , ρ is the mobile dislocation density, D_L is the temperature-dependent lattice self-diffusivity, k_b is the Boltzmann constant, and σ_d is the athermal detachment stress.

The relaxation factor k may be calculated from a series of creep experiments in which n_{app} , Q_{app} , and $\langle R \rangle$ are known:

$$k = 1 - \left(\frac{2k_B T}{3Gb^2\langle R \rangle} \cdot \frac{n_{app}}{(1 - \sigma/\sigma_d)^{1/2} \cdot \sigma/\sigma_d} \right)^{2/3} \quad (11)$$

The ratio σ/σ_d is given by:

$$\frac{\sigma}{\sigma_d} = \left(\frac{3(Q_{app} - Q)}{2RTn_{app}(1 - \frac{\partial G}{\partial T} \cdot \frac{T}{G})} + 1 \right)^{-1} \quad (12)$$

The value of k is between 0 and 1, with $k = 1$ indicating no attractive dislocation/particle interaction and $k < \sim 0.94$ being the threshold for which dislocation detachment becomes rate-limiting over dislocation climb processes in the limit of zero particle volume fraction [87]. This threshold value drops to $k < \sim 0.85$ for a particle volume fraction of 13%. Without considering the stress dependence of the mobile dislocation density ρ , as k approaches unity the stress dependence of the strain rate disappears, meaning Eq. (10) cannot be used to accurately describe the creep behavior in materials where there is no dislocation/particle attraction.

For the present AM Al-Ce-Ni-Mn alloy, $k = 0.99$ when using the measured values of n_{app} , Q_{app} , and $\langle R \rangle$, suggesting that dislocation/precipitate attractive interactions are small. The value of k does not change significantly with temperature or the value of Q_{app} used (189 or 264 kJ mol⁻¹, Fig. 6c). The weak dislocation/precipitate interaction implied by $k = 0.99$ agrees with other studies, where $k = 0.94-0.97$ was used to model the creep deformation of microstructurally similar Al-Fe-V-Si, Al-Fe-Ni, and Al-Fe-Ce alloys [77,80-82,84,85]. Thus, thermally activated dislocation detachment is not the rate-limiting mechanism in this AM Al-Ce-Ni-Mn alloy and Eq. (10) cannot be used to describe the creep behavior. This conclusion is supported by STEM imaging of creep samples, Fig. 7, in which the pinning of individual dislocations on the departure side of precipitates, a common signature of detachment-controlled creep [88], is not noted. Rather, networks of dislocations extend between the particles, forming a distinct subgrain structure. Rösler et al. attributed this type of microstructure to "matrix-like" creep where—like creep of a dispersion-free material—diffusion-controlled dislocation climb becomes rate-limiting, rather than detachment of dislocations from particles [88].

4.5.2. SKM constant structure model

To describe the creep behavior of dispersion-strengthened materials where diffusion-controlled dislocation climb is rate-limiting, the phenomenological SKM constant structure model may be used [79]. In this model, the strain rate at constant subgrain structure as determined by stress drop tests performed on pure materials is a function of the subgrain size:

$$\dot{\varepsilon} = K \left(\frac{\lambda_{cs}}{b} \right)^3 \frac{D_L}{b^2} \left(\frac{\sigma}{E} \right)^8 \quad (13)$$

where K is a constant equal to $\sim 10^9$ for materials with high stacking fault energy such as Al, E is the temperature-dependent elastic modulus, and λ_{cs} is the subgrain size (the cs subscript denotes "constant structure"). This phenomenological creep law assumes that all microstructural parameters remain constant, and that the creep deformation is limited by diffusion-controlled climb of dislocations around obstacles. Obstacles to free dislocation movement in pure materials include Frank dislocation networks within subgrains and the subgrain boundaries.

Sherby et al. have shown that Eq. (13) may also be used to describe diffusion-controlled steady-state creep behavior in dispersion-strengthened materials such as T-D Nichrome and Al-6Al₂O₃ (wt.%) [79,89], where the thermal stability of the dispersions constituted a constant structure during creep. The dispersions may restrict dislocation creep by (i) stabilizing a refined subgrain structure which is insensitive to stress and acts as a dislocation climb barrier and/or (ii) acting themselves as barriers to dislo-

Table 4

Summary of average precipitate radii $\langle R \rangle$ measured by microstructural analysis, interprecipitate spacings λ calculated from Eq. (7), and the ratio of threshold stress σ_{th} to the Orowan stress $\Delta\sigma_{Or}$ calculated from Eqs. (6) and (14) for several different creep temperatures. Radius values were measured after creep deformation, therefore the λ values correspond to the post-creep condition. Temperature dependence of the shear modulus G is taken from Ref. [48].

T (°C)	$\langle R \rangle$ (nm)	λ (nm)	$\Delta\sigma_{Or}$ (MPa)	$\frac{\sigma_{th}}{\Delta\sigma_{Or}}$
300	97 ± 17	93 ± 16	203 ± 49	0.14
350	162 ± 21	155 ± 20	131 ± 24	0.20
400	215 ± 55	205 ± 52	103 ± 37	0.17

cation climb. In the latter case, λ_{cs} then becomes equal to the interparticle spacing, i.e., λ in the Orowan equation, Eq. (6), for particle strengthening. Since STEM imaging of the crept microstructure in Fig. 7 shows subgrain diameters up to ~ 5 times larger than the average interparticle spacings, case (ii) is considered for the present AM Al-Ce-Ni-Mn alloy, as in studies on microstructurally similar Al-Fe-Ce and Al-Fe-V-Si alloys [83,86].

In Fig. 11a, the diffusivity-compensated strain rates are plotted vs. the modulus-compensated stresses for the experimental AM Al-Ce-Ni-Mn data, with Eq. (13) also plotted for several values of λ_{cs} . Fig. 11b further incorporates the influence of λ_{cs} on the strain rate. We plot the experimental data assuming λ_{cs} is equal to the interprecipitate spacing λ as calculated using Eq. (7) and measurements of $\langle R \rangle$. Calculated values of λ are shown in Table 4. When plotting the experimental data, we account for load transfer effects by multiplying the applied stress by the load transfer coefficient $\alpha_{LT} = 0.55$ from Eq. (8), thus reflecting the true stress applied to mobile dislocations. Fernández et al. demonstrated the validity of this approach in the analysis of Al metal matrix composite (MMC) creep behavior [90]. *In-situ* neutron or X-ray diffraction studies would be required to determine the precise level of load transfer but are beyond the present scope.

In general, the AM Al-Ce-Ni-Mn data show good agreement with the behavior predicted by Eq. (13), indicating that the dislocation creep behavior is diffusion-controlled, and that the effective interprecipitate spacing λ_{cs} is the primary microstructural factor influencing the creep behavior. Load transfer provided by the high volume fraction of precipitates also contributes by reducing the stress felt by mobile dislocations. The data at 300–350 °C collapse to the same iso- λ_{cs} line in Fig. 11a indicating that λ_{cs} is the same within this temperature range, even though the measured value of λ slightly increases during creep loading at 350 °C due to precipitate coarsening. The 400 °C curve falls along an iso- λ_{cs} line corresponding to higher λ_{cs} , perhaps reflective of the increasing interprecipitate spacing measured after creep loading. In prior creep studies of RS Al-Fe-Ce alloys, particle coarsening leading to a decrease in creep strength was observed at $T > 425$ °C [86,92]. The values of λ_{cs} corresponding to the measured creep behavior are lower than the λ values measured from microstructural analysis. The ratio λ/λ_{cs} is 4–6 at 300–350 °C and 2 at 400 °C. A similar observation was made by González-Doncel and Sherby for Al-SiC MMCs [93]. They proposed two possibilities for the discrepancy. The first possibility is that the value of A in Eq. (13) decreases when a high volume fraction of particles is present in the matrix since plastic deformation only occurs in the matrix portion of the composite, and $A = 10^9$ is determined from constant structure creep of pure aluminum. They found $A = 10^7$ to fit the experimental data well. When $A = 10^7$ is used it indeed fits the experimental AM Al-Ce-Ni-Mn data well by decreasing the model predictions by two orders of magnitude for a given normalized stress in Fig. 11. However, this explanation reduces A to a fitting factor, with a physical meaning that is unclear in terms of the creep behavior. The second proposed possibility is dislocation-dislocation inter-

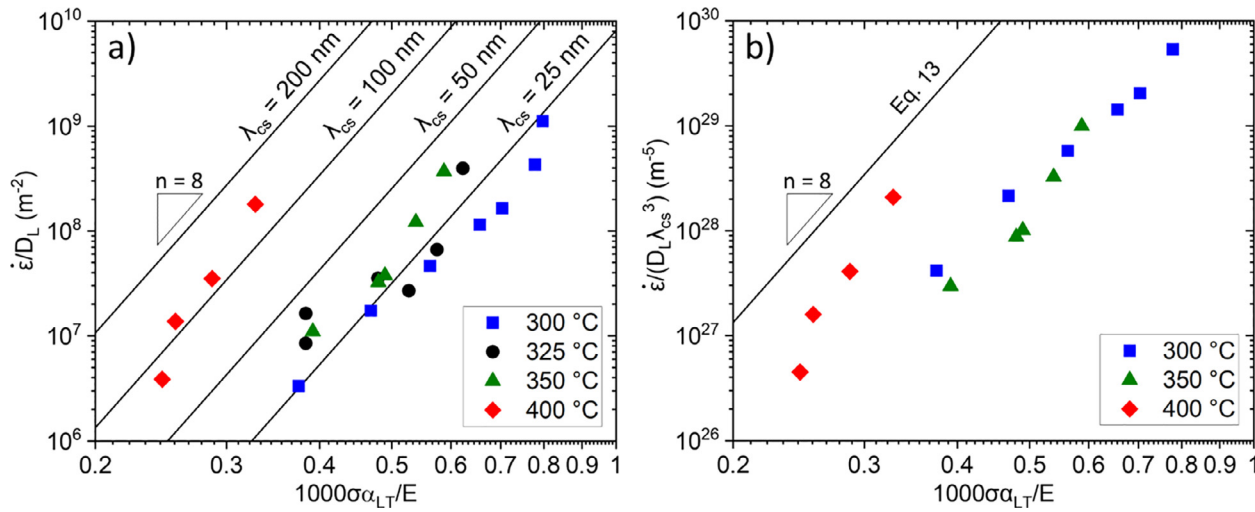


Fig. 11. AM Al-Ce-Ni-Mn creep data normalized to (a) the lattice diffusivity D_L and (b) the lattice diffusivity D_L and barrier spacing λ_{cs} , both plotted against modulus-compensated applied stress with a correction factor for load transfer effects α_{LT} . The straight lines are plotted according to Eq. (13). Temperature dependence of the modulus was taken from Ref. [91] and lattice diffusivity values are taken from Ref. [48]. When plotting the experimental data, the barrier spacings λ_{cs} are taken as the measured interprecipitate spacings λ from Table 4.

actions. Strain fields associated with dislocation networks formed around the precipitates effectively reduce the interprecipitate spacing, making the precipitates more effective barriers to dislocation motion. This theory was also postulated in discussions of Al-Fe-V-alloy creep behavior [83]. In the present AM Al-Ce-Ni-Mn alloy, dislocation structures around precipitates are indeed observed after creep, Fig. 7, and the prevalence of subgrain boundaries, whose strain fields may interact with moving dislocations [94], may also play a role in reducing the effective interprecipitate spacing.

When normalizing to λ_{cs}^3 in Fig. 11b, the experimental data are shifted relative to the model, again indicating $\lambda/\lambda_{cs} > 1$. The 400 °C data also remain shifted relative the 300–350 °C data indicating that, after accounting for temperature effects, the decrease in creep resistance at 400 °C is not solely due to an increase in λ_{cs} from precipitate coarsening. Considering that dislocation-dislocation interactions may be responsible $\lambda/\lambda_{cs} > 1$, it is possible that recovery processes that are more active at 400 °C cause λ/λ_{cs} to approach unity. Further *in situ* TEM studies during creep deformation would be required to confirm this hypothesis but are beyond the present scope.

Since the precipitates are likely acting as the primary barriers to diffusion-controlled dislocation climb, the threshold values as reported in Table 3 are related to the increase in dislocation line length needed for dislocations to climb over the precipitates. General climb, in which a portion of the dislocation line between adjacent precipitates climbs out of the slip plane while the dislocation is bypassing the precipitates, is more energetically favorable than local climb. During local climb the dislocation only climbs out of the slip plane directly at the matrix/precipitate interface, resulting in a greater increase in dislocation line length relative to general climb. Assuming general climb, the threshold stress is [95]:

$$\sigma_{th} = 0.4 \kappa \Delta\sigma_{0r} \quad (14)$$

where κ is the ratio of dislocation length increase for general climb to local climb, and is a function of the precipitate volume fraction [49]. For a volume fraction of 35% in the present alloy, $\kappa = 0.66$ and the ratio $\sigma_{th} / \Delta\sigma_{0r}$ should be 0.26 for a general climb mechanism, which is reasonably close to the ratios given in Table 4.

In addition to dislocation creep discussed thus far, diffusional creep is also relevant for alloys with small grain sizes, such as the

present alloy with grains on the order of 10–100 μm . Surprisingly, the AM Al-Ce-Ni-Mn alloy only exhibits diffusional creep at 400 °C for the stress levels investigated, implying that precipitates along grain boundaries are effective at restricting grain boundary diffusion and/or sliding in the 300–350 °C temperature range. We cannot determine the diffusional creep mechanism from the present data, as diffusional creep has only been observed at a single temperature and average grain size.

Finally, we discuss the differences in creep behavior between the AM Al-Ce-Ni-Mn alloy and other cast and PM alloys as shown in Fig. 6d. The AM Al-Ce-Ni-Mn alloy outperforms the three cast alloys, primarily because of differing volume fractions of strengthening precipitates. The Al-6.4Cu-0.19Mn-0.13Zr alloy [51] contains ~2–3 vol.% semi-coherent θ' -Al₂Cu precipitates which are effective barriers to dislocation motion, but their volume fraction is only ~7% of the precipitate volume fraction in AM Al-Ce-Ni-Mn. Furthermore, the thermal stability of the θ' is limited at $T > 350$ °C. The cast Al-0.10Sc-0.12Er alloy [52] has remarkable creep resistance per at.% solute in the alloy due to strong dislocation interactions with coherent and thermally stable L₁₂-Al₃(Sc,Er) nanoprecipitates, but their small volume fraction of < 0.5% limits the achievable creep resistance relative to AM Al-Ce-Ni-Mn. Although the volume fraction of thermally stable Al₁₁Ce₃ precipitates (11%) in cast Al-12.5Ce [50] is closer to AM Al-Ce-Ni-Mn, the interprecipitate spacings of ~1.5 μm are an order of magnitude larger, limiting the ability of the precipitates to block dislocation motion and decreasing the relative creep resistance.

Although the AM Al-Ce-Ni-Mn alloy has a higher volume fraction of precipitates than PM Al-Fe-V-Si [53] (35 vs. 27%) and comparable interprecipitate spacings, its creep resistance is lower at 300 °C. The higher creep resistance in PM Al-Fe-V-Si is likely because its Al₁₃(Fe,V)₃Si strengthening precipitates are coherent with the matrix, adding additional resistance to dislocation motion and enhancing dislocation-dislocation interactions. Furthermore, likely supersaturations of Fe and V in the matrix of PM Al-Fe-V-Si further restrict dislocation motion [53], whereas the matrix of AM Al-Ce-Ni-Mn is essentially pure Al, with the exception of 0.1 at.% Mn. In summary, the combination of the high volume fraction and submicron size of precipitates which provides load transfer and an effective barrier to dislocation motion, is key to the excellent creep resistance of the AM-Al-Ce-Ni-Mn alloy. These results contrast with existing creep studies of AM Al-Mg-Si and Al-Mg-Zr alloys.

4.6. Design considerations for creep-resistant AM Al alloys

The results from this study outline some important considerations in the design of creep-resistant AM Al alloys. The excellent creep resistance of the present AM Al-Ce-Ni-Mn alloy demonstrates that a high volume fraction of coarsening-resistant and refined phases as achievable during AM processing is a viable microstructural template for the design of future creep-resistant AM Al alloys. With the incorporation of modeling efforts and microstructural optimization enabled by additive manufacturing, the creep resistance may be further improved. For example, there are at least four different precipitate phases in the present alloy, Table S1, but it is unclear if any one type is significantly more coarsening-resistant or is a more effective barrier to dislocation motion. If phase-specific properties are elucidated (via *in-situ* nanoindentation, diffraction, or high-resolution microscopy) and appropriate thermodynamic and kinetic models are available, AM can be used to preferentially form an ensemble of the phases which are most coarsening- and creep-resistant. In the context of alloy printability for AM, identifying coarsening-resistant collections of phases that form during high-order eutectic reactions would also be a useful approach in alloy design, and may be accomplished by high-throughput thermodynamic calculations.

AM processing combined with heat treatments may also be used to tailor the precipitate morphology. In the present study the stress-relief heat treatment spheroidizes the as-fabricated microstructure with high-aspect ratio precipitates, Fig. 1. There is likely a resulting tradeoff between microstructural stability and load transfer, with low-aspect ratio precipitates being more resistant to coarsening and high-aspect ratio precipitates being more effective carriers of load. We have therefore maximized coarsening resistance at the expense of load transfer for the alloy microstructure presented in this study. Future studies aided by *in-situ* neutron or x-ray diffraction may be used to maximize the creep resistance within the context of the coarsening resistance/load transfer tradeoff.

Finally, the MPB structure in AM components is clearly a controlling factor in the creep lifetime, as evidenced by void formation along the MPBs during creep of the AM Al-Ce-Ni-Mn alloy, Fig. 10. AM processing may be utilized to tailor the MPB structure by changing the distribution and orientation of melt pools throughout the materials, or to control processing for selection of specific phases at the MPBs which are resistant to fracture or inhibit void nucleation. By building on the microstructural template for creep resistance herein, i.e., a high volume fraction of coarsening-resistant and refined phases, there are several avenues for design of creep-resistant AM Al alloys.

5. Conclusions

The additively manufactured Al-10.5Ce-3.1Ni-1.2Mn wt.% alloy studied herein is a promising high-temperature Al alloy. Through extensive characterization of the microstructure and mechanical behavior we make the following conclusions:

1. The as-stress-relieved microstructure of the alloy is complex, containing a high volume fraction (~35%) of spheroidized, submicron intermetallic phases. At least four different intermetallic phases are identified by atom-probe tomography. The compositions of the observed phases agree with thermodynamic calculations. The aluminum grains are largely columnar and aligned with the build direction, with grains ~10 μm wide and ~100 μm long.
2. The stress-relief anneal performed at 450 °C for 2 h creates a microstructure that is coarsening-resistant, as the initial average precipitate radius of 118 \pm 29 nm remains unchanged for

up to 200 h at 350 °C under load-free annealing. After 200 h of isothermal aging at 400 °C the average precipitate radius increases 17%. The coarsening resistance slightly decreases under creep loading conditions, with a 37% increase in precipitate radius observed after 312 h testing at 350 °C and an 82% increase in precipitate radius after 747 h testing at 400 °C.

3. The measured room-temperature yield strength of 258 \pm 4 MPa is close to the calculated yield strength accounting for grain boundary, solid solution, and Orowan strengthening, with an expected additional contribution from load transfer. An appreciable tensile ductility of 10 \pm 1% is obtained at room temperature. The yield strength at 400 °C is 70 \pm 1 MPa, ~60 MPa higher than AM Al-10Si-0.3Mg at that temperature. After stress-relief, the microhardness remains unchanged from ~110 HV after isothermal aging for 200 h at 300 and 350 °C. After 200 h aging at 400 °C, the microhardness slightly decreases by ~11%.
4. The creep resistance of the AM Al-10.5Ce-3.1Ni-1.2Mn alloy at 300–400 °C is superior to cast high-temperature Al alloys such as Al-12.5Ce, Al-6.4Cu-0.19Mn-0.13Zr, and Al-0.10Sc-0.12Er and is derived from the high volume fraction of coarsening-resistant submicron precipitates which are effective barriers to diffusion-controlled dislocation climb while also providing load transfer. These microstructural features are a template for design of future creep-resistant AM Al alloys. Diffusional creep is not observed at the stress levels investigated for $T \leq 350$ °C, suggesting that precipitates at grain boundaries are effective barriers to diffusional flow.
5. Lack of creep ductility (~2%) in the reported alloy is likely due to voids preferentially nucleating and growing on the MPBs, which are weaker regions in the material microstructure due to the formation of coarser intermetallic phases.

Declaration of Competing Interest

The authors declare no known competing financial or personal interests that could have appeared to influence the work reported in this manuscript.

Acknowledgments

Research was co-sponsored the U.S. Department of Energy, Office of Energy Efficiency and Renewable Energy, Advanced Manufacturing Office and Vehicle Technologies Office Propulsion Materials Program. APT was conducted at ORNL's Center for Nanophase Materials Sciences (CNMS), which is a U.S. DOE Office of Science User Facility. The authors would like to thank James Burns for assistance in performing APT sample preparation and running the APT experiments, Kelsey Hedrick and Shane Hawkins for performing the tensile tests, Dana McClurg for performing the heat treatments, Travis Dixon for electropolishing TEM samples, Christina Austin for assistance in performing the creep tests, and Sébastien Dryepondt and Yukinori Yamamoto for providing technical reviews of the manuscript.

References

- [1] R.A. Michi, A. Plotkowski, A. Shyam, R.R. Dehoff, S.S. Babu, Towards high-temperature applications of aluminium alloys enabled by additive manufacturing, *Int. Mater. Rev.* (2021) 1–48, doi:[10.1080/09506608.2021.1951580](https://doi.org/10.1080/09506608.2021.1951580).
- [2] S. Griffiths, J.R. Croteau, M.D. Rossell, R. Erni, A. De Luca, N.Q. Vo, D.C. Dunand, C. Leinenbach, Coarsening- and creep resistance of precipitation-strengthened Al-Mg-Zr alloys processed by selective laser melting, *Acta Mater.* (2020), doi:[10.1016/j.actamat.2020.02.008](https://doi.org/10.1016/j.actamat.2020.02.008).
- [3] N.E. Uzan, B. Ratzker, P. Landau, S. Kalabukhov, N. Frage, Compressive creep of AlSi10Mg parts produced by selective laser melting additive manufacturing technology, *Addit. Manuf.* 29 (2019) 100788, doi:[10.1016/j.addma.2019.100788](https://doi.org/10.1016/j.addma.2019.100788).
- [4] N.E. Uzan, R. Shneck, O. Yeheskel, N. Frage, High-temperature mechanical properties of AlSi10Mg specimens fabricated by additive manufacturing using selective laser melting technologies (AM-SLM), *Addit. Manuf.* 24 (2018) 257–263, doi:[10.1016/j.addma.2018.09.033](https://doi.org/10.1016/j.addma.2018.09.033).

- [5] C. Paoletti, E. Santecchia, M. Cabibbo, E. Cerri, S. Spigarelli, Modelling the creep behavior of an AlSi10Mg alloy produced by additive manufacturing, *Mater. Sci. Eng. A* (2020) 140138, doi:10.1016/j.msea.2020.140138.
- [6] J.H. Martin, B.D. Yahata, J.M. Hundley, J.A. Mayer, T.A. Schaebler, T.M. Pollock, 3D printing of high-strength aluminium alloys, *Nature* 549 (2017) 365–369, doi:10.1038/nature23894.
- [7] P. Mair, V.S. Goettgens, T. Rainer, N. Weinberger, I. Letofsky-Papst, S. Mitsche, G. Leichtfried, Laser powder bed fusion of nano-CaB₆ decorated 2024 aluminum alloy, *J. Alloy. Compd.* 863 (2021) 158714, doi:10.1016/j.jallcom.2021.158714.
- [8] P. Mair, L. Kaserer, J. Braun, N. Weinberger, I. Letofsky-Papst, G. Leichtfried, Microstructure and mechanical properties of a TiB₂-modified Al-Cu alloy processed by laser powder-bed fusion, *Mater. Sci. Eng. A* (2020) 140209, doi:10.1016/j.msea.2020.140209.
- [9] X. Liu, Y. Liu, Z. Zhou, K. Wang, Q. Zhan, X. Xiao, Grain refinement and crack inhibition of selective laser melted AA2024 aluminum alloy via inoculation with TiC-TiH₂, *Mater. Sci. Eng. A* 813 (2021) 141171, doi:10.1016/j.msea.2021.141171.
- [10] M. Opprecht, J.P. Garandet, G. Roux, C. Flament, M. Soulier, A solution to the hot cracking problem for aluminium alloys manufactured by laser beam melting, *Acta Mater.* (2020) S1359645420305139, doi:10.1016/j.actamat.2020.07.015.
- [11] J.R. Croteau, S. Griffiths, M.D. Rossell, C. Leinenbach, C. Kenel, V. Jansen, D.N. Seidman, D.C. Dunand, N.Q. Vo, Microstructure and mechanical properties of Al-Mg-Zr alloys processed by selective laser melting, *Acta Mater.* 153 (2018) 35–44, doi:10.1016/j.actamat.2018.04.053.
- [12] A.B. Spiersings, K. Dawson, T. Heeling, P.J. Uggowitzer, R. Schäublin, F. Palm, K. Wegener, Microstructural features of Sc- and Zr-modified Al-Mg alloys processed by selective laser melting, *Mater. Des.* 115 (2017) 52–63, doi:10.1016/j.matdes.2016.11.040.
- [13] R.S. Mishra, S. Thapliyal, Design approaches for printability-performance synergy in Al alloys for laser-powder bed additive manufacturing, *Mater. Des.* (2021) 109640, doi:10.1016/j.matdes.2021.109640.
- [14] A. Plotkowski, O. Rios, N. Sridharan, Z. Sims, K. Unocic, R.T. Ott, R.R. Dehoff, S.S. Babu, Evaluation of an Al-Ce alloy for laser additive manufacturing, *Acta Mater.* 126 (2017) 507–519, doi:10.1016/j.actamat.2016.12.065.
- [15] D.R. Manca, A.Y. Churyumov, A.V. Pozdniakov, A.S. Prosviryakov, D.K. Ryabov, A.Y. Krokhin, V.A. Korolev, D.K. Daubarayte, Microstructure and properties of novel heat resistant Al-Ce-Cu alloy for additive manufacturing, *Met. Mater. Int.* 25 (2019) 633–640, doi:10.1007/s12540-018-00211-0.
- [16] A. Plotkowski, K. Sisco, S. Bahl, A. Shyam, Y. Yang, L. Allard, P. Nandwana, A.M. Rossy, R.R. Dehoff, Microstructure and properties of a high temperature Al-Ce-Mn alloy produced by additive manufacturing, *Acta Mater.* 196 (2020) 595–608, doi:10.1016/j.actamat.2020.07.014.
- [17] K. Sisco, A. Plotkowski, Y. Yang, D. Leonard, B. Stump, P. Nandwana, R.R. Dehoff, S.S. Babu, Microstructure and properties of additively manufactured Al-Ce-Mg alloys, *Sci. Rep.* 11 (2021) 6953, doi:10.1038/s41598-021-86370-4.
- [18] L. Zhou, T. Huynh, S. Park, H. Hyer, A. Mehta, S. Song, Y. Bai, B. McWilliams, K. Cho, Y. Sohn, Laser powder bed fusion of Al-10 wt% Ce alloys: microstructure and tensile property, *J. Mater. Sci.* (2020), doi:10.1007/s10853-020-05037-z.
- [19] S. Thapliyal, S. Shukla, L. Zhou, H. Hyer, P. Agrawal, P. Agrawal, M. Komarasamy, Y. Sohn, R.S. Mishra, Design of heterogeneous structured Al alloys with wide processing window for laser-powder bed fusion additive manufacturing, *Addit. Manuf.* 42 (2021) 102002, doi:10.1016/j.addma.2021.102002.
- [20] G. Boussinot, M. Döring, S. Hemes, O. Stryzhyboroda, M. Apel, M. Schmidt, Laser powder bed fusion of eutectic Al Ni alloys: experimental and phase-field studies, *Mater. Des.* (2020) 109299, doi:10.1016/j.matdes.2020.109299.
- [21] J. Deng, C. Chen, X. Liu, Y. Li, K. Zhou, S. Guo, A high-strength heat-resistant Al-5.7Ni eutectic alloy with spherical Al₂Ni nano-particles by selective laser melting, *Scr. Mater.* 203 (2021) 114034, doi:10.1016/j.scriptamat.2021.114034.
- [22] X. Qi, N. Takata, A. Suzuki, M. Kobashi, M. Kato, Laser powder bed fusion of a near-eutectic Al-Fe binary alloy: processing and microstructure, *Addit. Manuf.* (2020) 101308, doi:10.1016/j.addma.2020.101308.
- [23] W. Wang, N. Takata, A. Suzuki, M. Kobashi, M. Kato, Formation of multiple intermetallic phases in a hypereutectic Al-Fe binary alloy additively manufactured by laser powder bed fusion, *Intermetallics* 125 (2020) 106892, doi:10.1016/j.intermet.2020.106892.
- [24] S. Sun, L. Zheng, H. Peng, H. Zhang, Microstructure and mechanical properties of Al-Fe-V-Si aluminum alloy produced by electron beam melting, *Mater. Sci. Eng. A* 659 (2016) 207–214, doi:10.1016/j.msea.2016.02.053.
- [25] A. Shyam, A. Plotkowski, S. Bahl, K. Sisco, L.F. Allard, Y. Yang, J.A. Haynes, R.R. Dehoff, An additively manufactured AlCuMnZr alloy microstructure and tensile mechanical properties, *Materialia* (2020) 100758, doi:10.1016/j.mtla.2020.100758.
- [26] S. Bahl, K. Sisco, Y. Yang, F. Theska, S. Primig, L.F. Allard, R.A. Michi, C. Fancher, B. Stump, R. Dehoff, A. Shyam, A. Plotkowski, Al-Cu-Ce-(Zr) alloys with an exceptional combination of additive processability and mechanical properties, *Addit. Manuf.* 48 (2021) 102404, doi:10.1016/j.addma.2021.102404.
- [27] N.T. Aboulkhair, M. Simonelli, L. Parry, I. Ashcroft, C. Tuck, R. Hague, 3D printing of aluminium alloys: additive manufacturing of aluminium alloys using selective laser melting, *Prog. Mater. Sci.* 106 (2019) 100578, doi:10.1016/j.pmatsci.2019.100578.
- [28] Q. Jia, F. Zhang, P. Rometsch, J. Li, J. Mata, M. Weyland, L. Bourgeois, M. Sui, X. Wu, Precipitation kinetics, microstructure evolution and mechanical behavior of a developed Al-Mn-Sc alloy fabricated by selective laser melting, *Acta Mater.* (2020) S135964542030272X, doi:10.1016/j.actamat.2020.04.015.
- [29] D.J. Skinner, R.L. Bye, D. Raybould, A.M. Brown, Dispersion strengthened Al-Fe-V-Si alloys, *Scr. Metall.* 20 (1986) 867–872, doi:10.1016/0036-9748(86)90456-4.
- [30] X. Qi, N. Takata, A. Suzuki, M. Kobashi, M. Kato, Change in microstructural characteristics of laser powder bed fused Al-Fe binary alloy at elevated temperature, *J. Mater. Sci. Technol.* (2021) S1005030221005004, doi:10.1016/j.jmst.2021.04.038.
- [31] X. Qi, N. Takata, A. Suzuki, M. Kobashi, M. Kato, Managing both high strength and thermal conductivity of a laser powder bed fused Al-2.5Fe binary alloy: effect of annealing on microstructure, *Mater. Sci. Eng. A* 805 (2021) 140591, doi:10.1016/j.msea.2020.140591.
- [32] N.A. Belov, E.A. Naumova, D.G. Eskin, Casting alloys of the Al-Ce-Ni system: microstructural approach to alloy design, *Mater. Sci. Eng. A* 271 (1999) 134–142, doi:10.1016/S0921-5093(99)00343-3.
- [33] E.J. Podnar, *Microstructural Evolution and Thermal Stability of Al-Ce-Ni Ternary Eutectic*, University of Florida, 2002.
- [34] F. Czerwinski, A search for the eutectic system of high-temperature cast aluminum alloys, *Mater. Sci. Technol.* (2021) 1–10, doi:10.1080/02670836.2021.1940670.
- [35] K.A. Jackson, J.D. Hunt, *Lamellar and rod eutectic growth*, *AIIM Met. Soc. Trans.* 236 (1966) 1129–1142.
- [36] M.K. Miller, K.F. Russell, G.B. Thompson, Strategies for fabricating atom probe specimens with a dual beam FIB, *Ultramicroscopy* 102 (2005) 287–298, doi:10.1016/j.ultramic.2004.10.011.
- [37] O.C. Hellman, J.A. Vandebroucke, J. Rüsing, D. Isheim, D.N. Seidman, Analysis of three-dimensional atom-probe data by the proximity histogram, *Microsc. Microanal.* 6 (2000) 437–444, doi:10.1007/S100050010051.
- [38] L. Kaufman, H. Bernstein, *Computer Calculation of Phase Diagrams With Special Reference to Refractory Metals*, Academic Press, Cambridge, Massachusetts, 1970.
- [39] A.T. Dinsdale, SGTE data for pure elements, *Calphad* 15 (1991) 317–425, doi:10.1016/0364-5916(91)90030-N.
- [40] H. Wang, Z. Li, Z. Chen, B. Yang, Thermodynamic optimization of the Ni-Al-Ce ternary system, *J. Ph. Equilib. Diffus.* 37 (2016) 222–228, doi:10.1007/s11669-015-0447-6.
- [41] Y. Yang, S. Bahl, K. Sisco, M. Lance, D. Shin, A. Shyam, A. Plotkowski, R.R. Dehoff, Primary solidification of ternary compounds in Al-rich Al-Ce-Mn alloys, *J. Alloy. Compd.* 844 (2020) 156048, doi:10.1016/j.jallcom.2020.156048.
- [42] Y. Yang, R.A. Michi, K. Sisco, R.R. Dehoff, Effect of Mn on eutectic phase equilibria in Al-rich Al-Ce-Ni alloys, *J. Alloy. Compd.* (2021).
- [43] E. Scheil, *Bemerkungen zur schichtkristallbildung*, *Z. Metall.* 34 (1942) 70–72.
- [44] D.J. Skinner, M.S. Zedalis, P. Gilman, Effect of strain rate on tensile ductility for a series of dispersion-strengthened aluminum-based alloys, *Mater. Sci. Eng. A* 119 (1989) 81–86, doi:10.1016/0921-5093(89)90526-1.
- [45] E. Bouchaud, L. Kubin, H. Octor, Ductility and dynamic strain aging in rapidly solidified aluminum alloys, *MTA* 22 (1991) 1021–1028, doi:10.1007/BF02661095.
- [46] J. Bi, Z. Lei, Y. Chen, X. Chen, Z. Tian, N. Lu, X. Qin, J. Liang, Microstructure, tensile properties and thermal stability of AlMgSiScZr alloy printed by laser powder bed fusion, *J. Mater. Sci. Technol.* (2020) S1005030220307398, doi:10.1016/j.jmst.2020.08.033.
- [47] T.H. Courtney, *Mechanical Behavior of Materials*, 2nd ed., Waveland Press, 2005.
- [48] H.J. Frost, M.F. Ashby, *Deformation Mechanism Maps: The Plasticity and Creep of Metals and Ceramics*, Pergamon Press, Oxford, UK, 1982 <http://publications.eng.cam.ac.uk/372960/> (accessed October 7, 2017).
- [49] M. McLean, On the threshold stress for dislocation creep in particle strengthened alloys, *Acta Metall.* 33 (1985) 545–556, doi:10.1016/0001-6160(85)90018-5.
- [50] Y. Liu, R.A. Michi, D.C. Dunand, Cast near-eutectic Al-12.5 wt% Ce alloy with high coarsening and creep resistance, *Mater. Sci. Eng. A* 767 (2019) 138440, doi:10.1016/j.msea.2019.138440.
- [51] B.K. Milligan, S. Roy, C.S. Hawkins, L.F. Allard, A. Shyam, Impact of microstructural stability on the creep behavior of cast Al-Cu alloys, *Mater. Sci. Eng. A* 772 (2020) 138697, doi:10.1016/j.msea.2019.138697.
- [52] R.A. Karnesky, D.N. Seidman, D.C. Dunand, Creep of Al-Sc microalloys with rare-earth element additions, *Mater. Sci. Forum* 519–521 (2006) 1035–1040, doi:10.4028/www.scientific.net/MSF.519-521.1035.
- [53] M. Zhang, R.J. Lewis, J.C. Gilling, Mechanisms of creep deformation in a rapidly solidified Al-Fe-V-Si alloy, *Mater. Sci. Eng. A* 805 (2021) 140796, doi:10.1016/j.msea.2021.140796.
- [54] K.E. Knipling, D.C. Dunand, D.N. Seidman, Criteria for developing castable, creep-resistant aluminum-based alloys—a review, *MEKU* 97 (2006) 246–265, doi:10.3139/146.101249.
- [55] C. Suwanpreecha, J.P. Toinin, R.A. Michi, P. Pandee, D.C. Dunand, C. Limmaneevichitr, Strengthening mechanisms in AlNiSc alloys containing Al₃Ni microfibers and Al₃Sc nanoprecipitates, *Acta Mater.* 164 (2019) 334–346, doi:10.1016/j.actamat.2018.10.059.
- [56] C. Suwanpreecha, P. Pandee, U. Patakham, C. Limmaneevichitr, New generation of eutectic Al-Ni casting alloys for elevated temperature services, *Mater. Sci. Eng. A* 709 (2018) 46–54, doi:10.1016/j.msea.2017.10.034.
- [57] R.A. Michi, J.P. Toinin, D.N. Seidman, D.C. Dunand, Ambient- and elevated-temperature strengthening by Al₃Zr-nanoprecipitates and Al₃Ni-microfibers in a cast Al-2.9Ni-0.11Zr-0.02Si-0.005Er (at.%) alloy, *Mater. Sci. Eng. A* 759 (2019) 78–89, doi:10.1016/j.msea.2019.05.018.

- [58] P. Pandey, S.K. Makineni, B. Gault, K. Chattopadhyay, On the origin of a remarkable increase in the strength and stability of an Al rich Al-Ni eutectic alloy by Zr addition, *Acta Mater.* 170 (2019) 205–217, doi:[10.1016/j.actamat.2019.03.025](https://doi.org/10.1016/j.actamat.2019.03.025).
- [59] F. Czerwinski, Thermal stability of aluminum-cerium binary alloys containing the Al-Al₁₁Ce₃ eutectic, *Mater. Sci. Eng. A* (2021) 140973, doi:[10.1016/j.msea.2021.140973](https://doi.org/10.1016/j.msea.2021.140973).
- [60] Z.C. Sims, O.R. Rios, D. Weiss, P.E.A. Turchi, A. Perron, J.R.I. Lee, T.T. Li, J.A. Hammons, M. Bagge-Hansen, T.M. Willey, K. An, Y. Chen, A.H. King, S.K. McCall, High performance aluminum-cerium alloys for high-temperature applications, *Mater. Horiz.* 4 (2017) 1070–1078, doi:[10.1039/C7MH00391A](https://doi.org/10.1039/C7MH00391A).
- [61] L. Angers, M.E. Fine, J.R. Weertman, Effect of plastic deformation on the coarsening of dispersoids in a rapidly solidified Al-Fe-Ce alloy, *MTA* 18 (1987) 555–562, doi:[10.1007/BF02649472](https://doi.org/10.1007/BF02649472).
- [62] Ø. Ryen, B. Holmedal, O. Nijls, E. Nes, E. Sjölander, H.E. Ekström, Strengthening mechanisms in solid solution aluminum alloys, *Metall. Mat. Trans. A* 37 (2006) 1999–2006, doi:[10.1007/s11661-006-0142-7](https://doi.org/10.1007/s11661-006-0142-7).
- [63] Z.C. Cordero, B.E. Knight, C.A. Schuh, Six decades of the Hall-Petch effect – a survey of grain-size strengthening studies on pure metals, *Int. Mater. Rev.* 61 (2016) 495–512, doi:[10.1080/09506608.2016.1191808](https://doi.org/10.1080/09506608.2016.1191808).
- [64] P.B. Hirsch, F.J. Humphreys, Plastic deformation of two-phase alloys containing small nondeformable particles, in: *The Physics and Strength of Plasticity*, MIT Press, Cambridge, MA, 1969, pp. 189–216.
- [65] M.A. Meyers, K.K. Chawla, *Mechanical Metallurgy: Principles and Applications*, Prentice-Hall, 1984.
- [66] E. Nembach, *Particle Strengthening of Metals and Alloys*, John Wiley & Sons, Inc., 1997.
- [67] K. Xia, X. Wu, Back pressure equal channel angular consolidation of pure Al particles, *Scr. Mater.* 53 (2005) 1225–1229, doi:[10.1016/j.scriptamat.2005.08.012](https://doi.org/10.1016/j.scriptamat.2005.08.012).
- [68] S.H. Hong, K.H. Chung, High temperature creep behavior of SiC/2124Al metal matrix composites, *Key Eng. Mater.* 104–107 (1995) 757–764, doi:[10.4028/www.scientific.net/KEM.104-107.757](https://doi.org/10.4028/www.scientific.net/KEM.104-107.757).
- [69] V.C. Nardone, K.M. Prewo, On the strength of discontinuous silicon carbide reinforced aluminum composites, *Scr. Metall.* 20 (1986) 43–48, doi:[10.1016/0036-9748\(86\)90210-3](https://doi.org/10.1016/0036-9748(86)90210-3).
- [70] H. Sekine, R. Chent, A combined microstructure strengthening analysis of SiCp/Al metal matrix composites, *Composites* (1995) 183–188.
- [71] Q. Guo, Y. Han, D. Zhang, Interface-dominated mechanical behavior in advanced metal matrix composites, *Nano Mater. Sci.* 2 (2020) 66–71, doi:[10.1016/j.nanoms.2020.03.007](https://doi.org/10.1016/j.nanoms.2020.03.007).
- [72] T. Uesugi, K. Higashi, First-principles studies on lattice constants and local lattice distortions in solid solution aluminum alloys, *Comput. Mater. Sci.* 67 (2013) 1–10, doi:[10.1016/j.commatsci.2012.08.037](https://doi.org/10.1016/j.commatsci.2012.08.037).
- [73] J. Delahaye, J.T. Tchuindjang, J. Lecomte-Beckers, O. Rigo, A.M. Habraken, A. Mertens, Influence of Si precipitates on fracture mechanisms of AlSi10Mg parts processed by Selective Laser Melting, *Acta Mater.* 175 (2019) 160–170, doi:[10.1016/j.actamat.2019.06.013](https://doi.org/10.1016/j.actamat.2019.06.013).
- [74] D.D. Ben, Y.R. Ma, H.J. Yang, L.X. Meng, X.H. Shao, H.Q. Liu, S.G. Wang, Q.Q. Duan, Z.F. Zhang, Heterogeneous microstructure and voids dependence of tensile deformation in a selective laser melted AlSi10Mg alloy, *Mater. Sci. Eng. A* 798 (2020) 140109, doi:[10.1016/j.msea.2020.140109](https://doi.org/10.1016/j.msea.2020.140109).
- [75] Z.H. Xiong, S.L. Liu, S.F. Li, Y. Shi, Y.F. Yang, R.D.K. Misra, Role of melt pool boundary condition in determining the mechanical properties of selective laser melting AlSi10Mg alloy, *Mater. Sci. Eng. A* 740–741 (2019) 148–156, doi:[10.1016/j.msea.2018.10.083](https://doi.org/10.1016/j.msea.2018.10.083).
- [76] S. Bahl, A. Plotkowski, K. Sisco, D.N. Leonard, L.F. Allard, R.A. Michi, J.D. Poplawsky, R. Dehoff, A. Shyam, Elevated temperature ductility dip in an additively manufactured Al-Cu-Ce alloy, *Acta Mater.* 220 (2021) 117285, doi:[10.1016/j.actamat.2021.117285](https://doi.org/10.1016/j.actamat.2021.117285).
- [77] J. Rösler, E. Arzt, A new model-based creep equation for dispersion strengthened materials, *Acta Metall. Mater.* 38 (1990) 671–683, doi:[10.1016/0956-7151\(90\)90223-4](https://doi.org/10.1016/0956-7151(90)90223-4).
- [78] E. Arzt, J. Rösler, The kinetics of dislocation climb over hard particles—II. Effects of an attractive particle-dislocation interaction, *Acta Metall.* 36 (1988) 1053–1060, doi:[10.1016/0001-6160\(88\)90159-9](https://doi.org/10.1016/0001-6160(88)90159-9).
- [79] O.D. Sherby, R.H. Klundt, A.K. Miller, Flow stress, subgrain size, and subgrain stability at elevated temperature, *MTA* 8 (1977) 843–850, doi:[10.1007/BF02661565](https://doi.org/10.1007/BF02661565).
- [80] F. Carreño, O.A. Ruano, Separated contribution of particles and matrix on the creep behavior of dispersion strengthened materials, *Acta Mater.* 46 (1998) 159–167, doi:[10.1016/S1359-6454\(97\)00217-6](https://doi.org/10.1016/S1359-6454(97)00217-6).
- [81] S. Mitra, Elevated temperature deformation behavior of a dispersion-strengthened Al-Fe,V,Si alloy, *MMTA* 27 (1996) 3913–3923, doi:[10.1007/BF02595640](https://doi.org/10.1007/BF02595640).
- [82] L.M. Peng, S.J. Zhu, Z.Y. Ma, J. Bi, H.R. Chen, F.G. Wang, High temperature creep deformation of an Al-Fe-V-Si alloy, *Mater. Sci. Eng. A* 259 (1999) 25–33, doi:[10.1016/S0921-5093\(98\)00876-4](https://doi.org/10.1016/S0921-5093(98)00876-4).
- [83] J. Wolfenstein, G. Gonzalez-Doncel, O.D. Sherby, Deformation behaviour under constant structure of creep-resistant Al-Fe alloys, *J. Mater. Sci. Lett.* 9 (1990) 410–413, doi:[10.1007/BF00721014](https://doi.org/10.1007/BF00721014).
- [84] F. Dobeš, Interpretation of the creep behaviour of dispersion-strengthened Al-Fe-Ni alloys in terms of the detachment mechanism, *Mater. Sci. Eng. A* 194 (1995) L19–L21 A.
- [85] M.K. Premkumar, A. Lawley, M.J. Koczak, Mechanical behavior of powder metallurgy Al-Fe-Ni alloys, *Mater. Sci. Eng. A* A174 (1994) 127–139, doi:[10.1016/0921-5093\(94\)91081-2](https://doi.org/10.1016/0921-5093(94)91081-2).
- [86] D. Legzdina, T.A. Parthasarathy, Deformation mechanisms of a rapidly solidified Al-8.8Fe-3.7Ce alloy, *Metall. Trans. A* 18A (1987) 1713–1719.
- [87] E. Arzt, D.S. Wilkinson, Threshold stresses for dislocation climb over hard particles: the effect of an attractive interaction, *Acta Metall.* 34 (1986) 1893–1898.
- [88] J. Rösler, R. Joos, E. Arzt, Microstructure and creep properties of dispersion-strengthened aluminum alloys, *MTA* 23 (1992) 1521–1593, doi:[10.1007/BF02647335](https://doi.org/10.1007/BF02647335).
- [89] J. Lin, O.D. Sherby, Creep of oxide dispersion strengthened materials (with special reference to T.D. Nichrome), *Res. Mech.* 2 (1981) 251–293.
- [90] R. Fernández, G. González-Doncel, Threshold stress and load partitioning during creep of metal matrix composites, *Acta Mater.* 56 (2008) 2549–2562, doi:[10.1016/j.actamat.2008.01.037](https://doi.org/10.1016/j.actamat.2008.01.037).
- [91] L.F. Mondolfo, *Aluminum Alloys: Structure and Properties*, Butterworths, 1976.
- [92] R.K. Mahidhara, Degradation of RSP/PM Al-8Fe-4Ce during creep, *JMEP* 5 (1996) 256–259, doi:[10.1007/BF02650896](https://doi.org/10.1007/BF02650896).
- [93] G. González-Doncel, O.D. Sherby, High temperature creep behavior of metal matrix aluminum-SiC composites, *Acta Metall. Mater.* 41 (1993) 2797–2805, doi:[10.1016/0956-7151\(93\)90094-9](https://doi.org/10.1016/0956-7151(93)90094-9).
- [94] M.E. Kassner, M.T. Pérez-Prado, Five-power-law creep in single phase metals and alloys, *Prog. Mater. Sci.* 45 (2000) 1–102, doi:[10.1016/S0079-6425\(99\)00006-7](https://doi.org/10.1016/S0079-6425(99)00006-7).
- [95] A.M. Jansen, D.C. Dunand, Creep of metals containing high volume fractions of unshearable dispersoids—Part II. Experiments in the Al-Al₂O₃ system and comparison to models, *Acta Mater.* 45 (1997) 4583–4592, doi:[10.1016/S1359-6454\(97\)00136-5](https://doi.org/10.1016/S1359-6454(97)00136-5).